Materials Science and Engineering B 192 (2015) 3–25

Contents lists available at ScienceDirect

Materials Science and Engineering B

journal homepage: www.elsevier.com/locate/mseb

Review

Fundamental degradation mechanisms of layered oxide Li-ion battery cathode materials: Methodology, insights and novel approaches

R. Hausbrand*, G. Cherkashinin, H. Ehrenberg, M. Gröting, K. Albe, C. Hess, W. Jaegermann

SFB 595, Institute of Materials Science and Institute of Physical Chemistry, Technical University of Darmstadt, Alarich-Weiss-Str. 2, 64287 Darmstadt, Germany

ARTICLE INFO

Article history:
Received 2 July 2014
Received in revised form 3 November 2014
Accepted 12 November 2014
Available online 27 November 2014

ABSTRACT

This overview addresses the atomistic aspects of degradation of layered $LiMO_2$ (M = Ni, Co, Mn) oxide Li-ion battery cathode materials, aiming to shed light on the fundamental degradation mechanisms especially inside active cathode materials and at their interfaces. It includes recent results obtained by novel *in situ*/*in operando* diffraction methods, modelling, and quasi *in situ* surface science analysis. Degradation of the active cathode material occurs upon overcharge, resulting from a positive potential shift of the anode. Oxygen loss and eventual phase transformation resulting in dead regions are ascribed to changes in electronic structure and defect formation. The anode potential shift results from loss of free lithium due to side reactions occurring at electrode/electrolyte interfaces. Such side reactions are caused by electron transfer, and depend on the electron energy level alignment at the interface. Side reactions at electrode/electrolyte interfaces and capacity fade may be overcome by the use of suitable solid-state electrolytes and Li-containing anodes.

Contents

* Corresponding author. Tel.: +49 6151 1670836; fax: +49 6151 166308.
E-mail address: hausbrand@surface.tu-darmstadt.de (R. Hausbrand).

http://dx.doi.org/10.1016/j.mseb.2014.11.014

1. Introduction

Electric energy on demand and without evident emissions or network connections is urgently needed (see [1]). Mobile applications require advanced batteries providing higher power and energy density, but at the same time fulfilling the highest safety standards. In addition, fossil fuels will probably be substituted by renewable energy sources such as wind and solar, which are characterized by their volatility. Thus, for stationary applications more efficient storage devices are also required (see [2]), *i.e.* for load-levelling or island-type storage solutions, providing high reliability and long term stability.

Although Li-ion batteries are promising systems for such large scale energy storage solutions, stability issues and degradation phenomena are impeding their application and further development. In this context, the cathode plays a key role for capacity, safety and the cycle life [3]. Despite substantial effort in the past to shed light on fundamental degradation processes, generally no common understanding has been achieved and investigations are ongoing, the main difficulty being the evaluation of material and interface properties on a microscopic or atomic scale. These issues were therefore addressed as a main research topic of a collaborative research effort (DFG SFB 595). Central were investigations that result in an atomistic view on degradation and fatigue, specifically regarding changes inside cathode materials and at their interfaces caused by parasitic electronic and ionic defect formation and coupled transfer reactions.

Particularly, this contribution focuses on the atomistic aspects of degradation of layered oxide Li-ion cell cathode materials such as $LiCoO_2$ and their interfaces. After recalling fundamentals regarding Li-ion cells and their degradation, we introduce our specific experimental approach to evaluate degradation of active material on atomic and microscopic scale using *in situ*/*in operando* diffraction, modelling and quasi *in situ* surface science investigations. In the following three sections, we present recent results regarding the evolution of structural changes, defect formation, and electronic structure, each section including background with relevant literature as well as discussion. The subsequent section deals with degradation on cell and component level, presenting recent results and demonstrating the causes for the degradation of active cathode material. Following, solid electrolytes and related cells are introduced as a new approach to overcome interface reactivity and capacity fade.

2. Fundamentals and definitions

2.1. Rocking chair batteries

In a standard arrangement Li-ion intercalation batteries operate according to the "rocking-chair" principle (see e.g. [2,4]). The Li-ions are transferred between two materials which can incorporate (intercalate) the Li-ions into non-occupied lattice sites coupled to electron transfer into unoccupied electronic states of the solid. See Fig. 1 for an illustration of cell operation.

During charging of the cell, the Li-ion and electron flux is directed towards the negative electrode (anode), and during discharge towards the positive electrode (cathode). For a typical

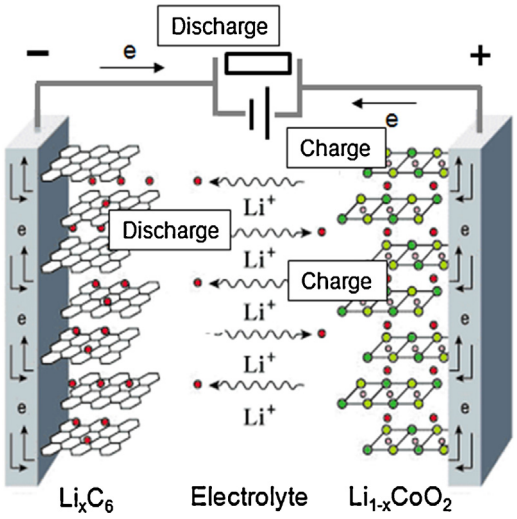

Fig. 1. Illustration of Li-ion cell. During operation, Li-ions are shuttled back and forth between Li-intercalation electrodes ("rocking chair" principle). Specifically, during charging lithium ions and electrons are transferred from the positive layered oxide electrode (cathode) to the negative carbon electrode (anode).

layered oxide cathode and a carbon anode the overall discharge exchange reaction can be written as (M: transition metal):

$$Li_xC_6 + Li_{1-x}MO_2 \underset{\text{Charge}}{\overset{\text{Discharge}}{\rightleftharpoons}} C_6 + LiMO_2 \quad (1)$$

Ideally, only Li-ions are transferred across the electrode/electrolyte interfaces. Transfer of electrons constitutes side reactions leading to self-discharge and degradation.

As cathode materials layered oxides $LiMO_2$ or spinel type LiM_2O_4 compounds (lithium-containing transition metal oxides, with M = Co, Ni, Mn of different composition) have mostly been used, but also $LiMPO_4$ compounds (lithium-containing transition metal phosphates and similar compounds such as silicates) are increasingly popular [4]. Fig. 2 shows schematically the crystal- and electronic structure of $LiMO_2$ cathode materials. Depending on the sequence of the O—M—O layers different polytypes can occur [4]. The approximately octahedrally coordinated environment of the transition metal ions can show structural distortion induced by the Jahn-Teller effect. Moreover, there are strong structural changes observed upon changes of lithium content (depending on type, composition and distribution of the transition metals) which strongly influence the bulk structural properties and the electrochemical potentials.

For idealized conditions (bulk materials) the reversible cell voltage (open circuit voltage V_{OC}, electromotoric force, EMF) is given by the chemical potential (μ) difference of Li-atoms between cathode and anode [7]:

$$-eV_{OC} = \mu_{Li,Cathode} - \mu_{Li,Anode} \quad (2)$$

From a chemical point of view, the reversible cell voltage may be approximated by the difference in the redox potential for Li^+/Li of the anode (neglecting the minor influence of the carbon host on the potential) to the potential of the operating transition metal ion

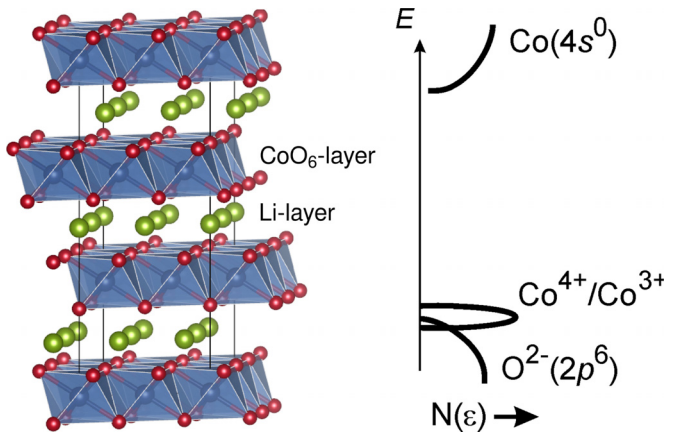

Fig. 2. Crystal structure (left) and schematic electronic structure (right) of Li_xCoO_2 (see [5,6]). During delithiation, lithium ions and electrons are removed from the host lattice. Removal of electrons is highly localized to cobalt ions, but also affects the band structure.

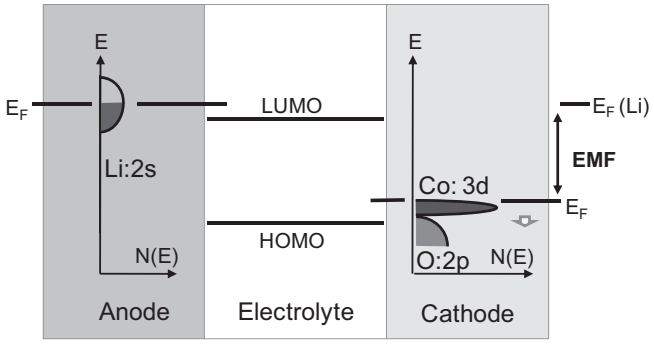

Fig. 3. Schematic energy level diagram for lithium cell with $LiCoO_2$ as cathode and lithium as anode, illustrating the origin of the EMF. The Fermi level of the lithium anode is drawn above the LUMO of the electrolyte, indicating reduction of the electrolyte as usually observed. Note that the Fermi level of the cathode shifts downwards during deintercalation, as indicated by the small arrow.

redox-couple in the oxide cathode, *e.g.* such as Co^{4+}/Co^{3+} in $LiCoO_2$. This potential is strongly influenced by the inductive effect of the other ions and their effective charge in the lattice [5].

Alternatively, from a physical point of view, one may relate the cell voltage to the difference of the (electro-)chemical potential of the electrons between the cathode and anode as given by the position of their Fermi levels (see Fig. 3). Note, however, that the chemical potential difference of lithium between anode and cathode may be expressed as the sum of the chemical potential difference for both electrons ($\Delta\mu_{e}-$) and ions ($\Delta\mu_{Li+}$) [7,8]:

$$-eV_{OC} = \Delta\mu_{e^-} + \Delta\mu_{Li^+} \quad (3)$$

Therefore, considerations restricted to the Fermi level (electron chemical potential) of (single) electrode materials in discussion of electrode potentials are approximate, albeit often resulting in reasonable accuracy.

Besides the active (intercalation) material, commercial Li-ion electrodes consist of polymer binder and conductive additives, forming complex, often nano-sized, 2-D or 3D composites. The performance of these composite electrodes is highly dependent on the distribution, ratio and type of the different constituents [9,10]. From an idealized point of view, voltage and capacity of Li-ion batteries are only determined by the thermodynamic bulk properties of the active phases, as discussed. However, in real batteries, contact potentials and kinetic effects strongly influence the practically achieved voltages, capacities and current densities. As a consequence, all practical performance data (*e.g.* energy and power density, lifetime) are influenced by kinetic factors, which are often dominated by interface effects, and continually evolve with time due to side reactions and other degradation phenomena [11].

2.2. Fatigue, ageing and cell failure

Degradation is mainly characterized by irreversible capacity loss (capacity fade) and voltage loss, *i.e.* increase in cell impedance (Fig. 4), coupled to changes in kinetic and thermodynamic

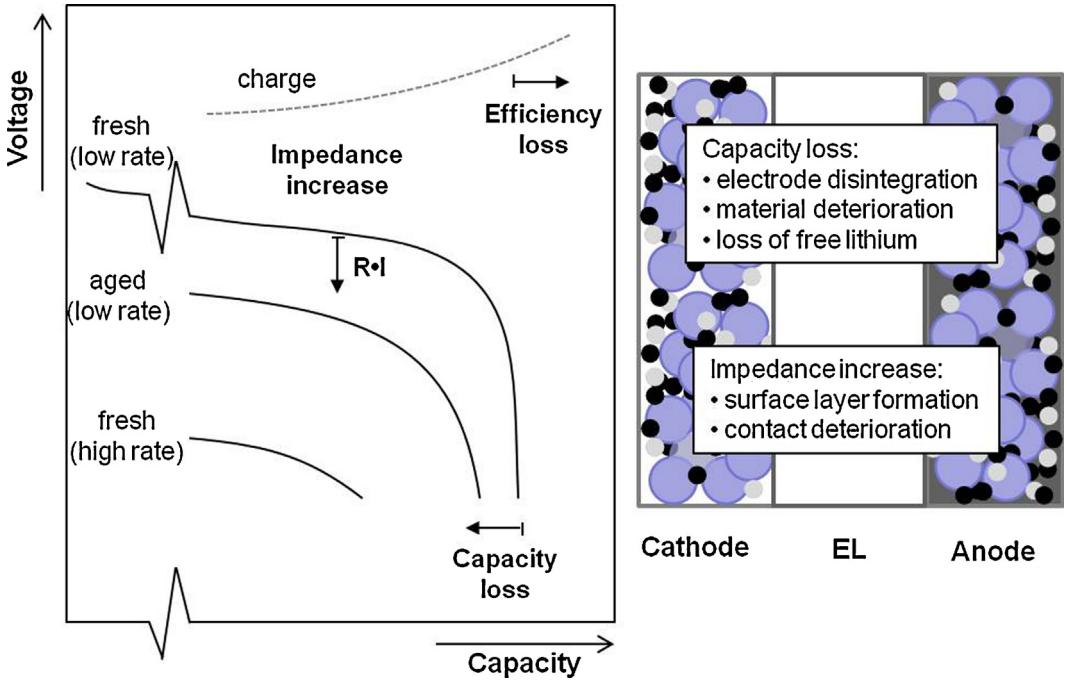

Fig. 4. Degradation as observed in discharge curves (left) and major causes for degradation of Li-ion batteries (right, EL denotes electrolyte). Side reactions at internal and external interfaces play a major role for degradation, resulting in loss of free lithium and impedance increase.

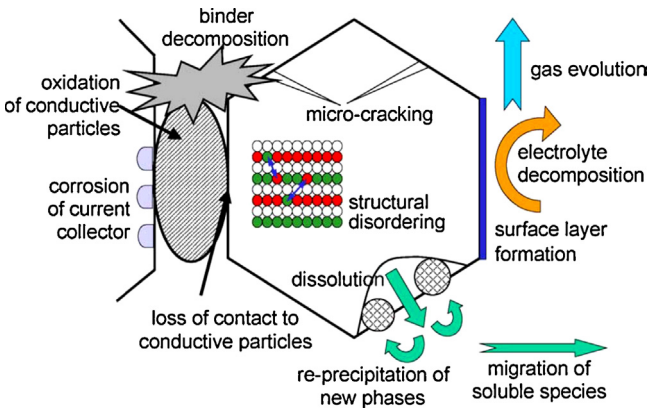

Fig. 5. Degradation mechanisms of composite cathodes. Reprinted from [11] with permission from Elsevier.

properties of involved materials and their interfaces (see *e.g.* [11]). Degradation is caused by fatigue during cell operation (charge/discharge cycles) as well as ageing phenomena occurring at rest conditions.

Li-ion batteries are thermodynamically very unstable systems, allowing for (electro-)chemical side reactions and phase changes during operation and at rest. The life time of a battery can be divided into three parts: (1) formation during the first cycles, (2) normal operation and (3) the end of life (EOL). The operation of Li-ion cells takes place outside the stability window of the electrolyte. Ongoing electrolyte reduction at the negative electrode is stopped during formation by an electronically insulating solid-electrolyte interphase (SEI). The detailed conditions during formation, like temperature and cut-off voltages, play a crucial role for the performance parameters of the device during the following operation [12]. They define the amount of irreversible capacity loss during formation and the accessible capacity for successive operation. Furthermore, the SEI is mainly responsible for the state of fatigue and therefore for the lifetime of the device. The formation of SEI-layers must also be considered for the positive electrode, however its thickness is much smaller than on the anode side. The end-of-life (EOL) criteria are a residual capacity of only 80% of its initial value after formation or a 30% increase of the internal resistance. Capacity losses are partially caused by the formation of "dead lithium", meaning lithium dendrites, which have lost electronic contact to the negative electrode.

Many degradation phenomena have to be considered on component level, such as loss of contact between particles, cracking of particles, point defect formation as well as structural changes inside the active materials and interface reactions [11], such as shown in Fig. 5 for composite cathodes.

On the atomistic scale, degradation can in first instance be described as the evolution of point defects in the volume of the materials as well as the evolution of reaction layers at surfaces and interfaces. Defect formation and transport are a function of various parameters such as the electric field, mechanical strain and temperature, which periodically change during cycling. Defects and surface layers of active electrode materials are formed during material synthesis and continuously evolve during the lifetime of the materials. While the evolution of volume defects takes place only on long time scales due to high activation energies, surface layers are typically formed on short time scales immediately after exposure to a new phase or different environment. Therefore, handling and formation are crucial for surface layer formation.

The point defect formation inside active cathode materials is coupled to its electronic structure and Fermi level position. The Fermi level position reflects the stability limits of oxide cathode materials with respect to the degree of lithiation. As a consequence, detailed understanding regarding change of Fermi level position and electronic structure itself with charging (deintercalation) and discharging (intercalation) of the cathodes is of foremost importance for degradation phenomena. An intrinsic limit of degradation will therefore be reached when the chemical potential of electrons (or holes, respectively) will reach a position where side reactions, such as oxidation of O^{2-} – lattice sites, will interfere with metal-ion electron exchange reactions. In addition, the position of the electrode Fermi level with respect to the energy states of HOMO and LUMO in the electrolyte defines if electron or hole transfer induced chemical reactions may occur (see Fig. 3).

2.3. Interfaces

Further improvements of electrodes and cells are limited by an incomplete understanding of interfaces, the involved charge transfer, charge compensation and chemical reaction processes which are characterized by directional and mostly opposing transport of electronic and ionic charge carriers. Thus a detailed understanding of the role of the different interfaces involved is a necessary precondition for developing highly stable, next generation Li-ion batteries. The contact properties – determined by the solid electrolyte interphase or SEI layers – between the active electrode material and the electrolyte are thereby of key relevance [13,14], especially for future high voltage cathodes. Interfaces between ionic conductors, exhibiting different values of the electrochemical potentials of mobile ions, induce charge transfer and the formation of space charge or double layers to obtain ionic equilibrium [15,16]. It has been proven by a number of studies mainly on nano-sized systems that the aforementioned electrified interfaces often dominate the macroscopic behaviour of ionic systems, and that these effects may be exploited for new device structures (*Nanoionics*) [17,18]. So far, however, there is only limited information on the composition and interface related structural and electronic properties within the electrodes (anodes and cathodes) including the contact properties between electrodes and electrolyte. Electronic energy level diagrams of Li-ion batteries have been schematically introduced [5,6,19], but have remained mostly conceptual with hardly any detailed or experimentally based data about the contact potential distribution needed to assess charge transfer phenomena, defect formation and interface layer stabilities in real systems.

3. Methodology

Various analytical methods and approaches have been used to investigate degradation on different levels, *i.e.* on full cells, components and model systems, such as neutron radiography, X-ray diffraction or tomography, transmission electron spectroscopy, optical spectroscopy, photoelectron spectroscopy and X-ray absorption spectroscopy [14,20–25]. Similarly, various simulation tools have been employed. In the following section, tools and approaches will be introduced that proved most useful in understanding degradation phenomena.

3.1. In situ X-ray and in operando neutron diffraction

Structural changes during fatigue need to be monitored under exactly the same conditions as in normal operation, because any change in the highly reactive electrolyte environment of the electrochemically active materials during sample preparation could falsify the relevant degradation mechanisms. While transport behaviour is mainly affected by the surface near regions, pronounced capacity losses must also have a significant contribution from volume effects.

X-ray and neutron diffraction are suitable methods to monitor structural changes in dependence on state-of-charge (SOC) and state-of-health (SOH) [26]. Two obvious effects can be detected easily: (1) lattice strain as a consequence of bond-length variations, caused by successive oxidation and reduction of transition metals and occupation or depopulation of Li sites; (2) broad dead regions, which do not participate anymore in the redox reactions, either because of contact loss or other deactivation mechanisms. (1) is reflected in changes of the unit cell metric, determined from the positions of reflections of the underlying crystal structure. (2) is detected and quantified from the phase ratio of passive amounts, identified as phases, which do not show any shift in the positions of the reflections. All relevant positive electrode materials show significant changes in the lattice parameters with changes in the SOC, so that both aspects (1) and (2) can be addressed by diffraction experiments, using X-ray, synchrotron or neutron diffraction.

However, very good diffraction data are needed, which allow a reliable interpretation of shifts in the positions of reflections and changes in both half widths and profiles of reflections. It is the instrumental resolution function of an experimental setup, which defines the detection limit for these changes. Therefore, much smaller effects can be revealed by the use of a high-resolution setup at a synchrotron source, while only more pronounced changes can be analyzed in diffraction experiments with lower angular resolution. Lattice parameters are derived from Rietveld refinements of structure models, adapted to converge at the best agreement between the simulated patterns in comparison with experimental data.

For reliable determinations of lattice parameters experiments in transmission geometry are highly recommended, maybe even essential. High energies of X-rays or neutron radiation are needed to guarantee a sufficiently good penetration capability to probe the full volume and detect the transmitted beam with good counting statistics. Note, that position-sensitive detectors (PSDs) are needed, which cover the full range of diffraction angles simultaneously, because non-equilibrium conditions are measured. The state of the sample changes with time, and a combination of consecutively recorded diffraction data into one pattern is not possible. Both 1- or 2-dimensional PSDs can be used, depending on the specific preference for angular *vs.* time resolution [27,28].

Several generations of transmission *in situ* test cells were developed with a minimum of scattering from shielding and passive components and a very good sealing, which is essential for high cycle numbers to study fatigue, *e.g.* [28–30]. Three successive generations of electrochemical *in situ* cells for X-ray diffraction are shown in Fig. 6.

Complete devices with sizes of 1 cm and more can be studied with dedicated setups, like realized at the neutron powder diffractometer SPODI [31]. This allows for *in operando* studies on 18650-type cells, and fatigue can be studied under exactly the same conditions as in the established applications of Li-ion batteries [32]. Neutron diffraction has one more advantage against X-ray and even high-energy synchrotron radiation: The light elements, like H, Li, C, O and F, which are important components in battery materials, are well localized within structure models, because of the much stronger scattering power of these elements for neutrons than for photons.

3.2. *In situ* Raman spectroscopy

As an optical method Raman spectroscopy has the potential to study electrode materials under *in situ* conditions [33,34].

To increase the sensitivity of the method and to provide a basis for spatially resolved *in situ* analysis of cathode materials, resonance enhancements can be exploited [34,35]. While the presence of resonance Raman effects in Li-ion battery cathode materials

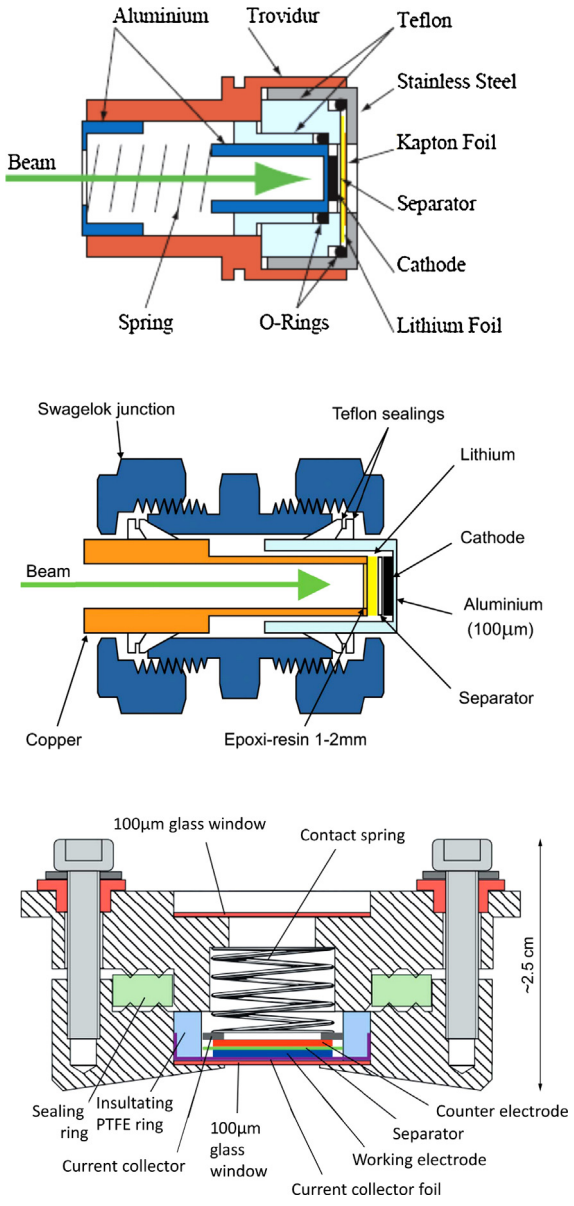

Fig. 6. Schematic drawing of electrochemical *in situ* cells. Top: reprinted from [29] with permission from Elsevier. Middle, bottom: reproduced from [28,30] with permission of the International Union of Crystallography.

has been reported for $LiNi_xMn_{2-x}O_4$ [36], $LiNi_{0.8}Co_{0.15}Al_{0.05}O_2$ and $LiNi_{1/3}Co_{1/3}Mn_{1/3}O_2$ [37], we recently demonstrated, for the first time, the resonance enhancement of $LiCoO_2$ materials using wavelength dependent studies [34]. Fig. 7 shows 514.5, 532 and 632.8 nm Raman data of as prepared $LiCoO_2$. Changing the laser excitation wavelength from red to green results in an increase of the A_{1g} (595 cm^{-1})/E_g (485 cm^{-1}) intensity ratio and the occurrence of an overtone of the A_{1g} band. Such behaviour is fully consistent with a resonance Raman effect based on a term A enhancement [38].

3.3. *Surface analysis*

The electronic structure and chemical composition of cathode surfaces and interfaces is frequently analyzed by photoemission (PES, *i.e.* X-ray and ultraviolet photoelectron spectroscopy, XPS and UPS) and related techniques such as X-ray absorption spectroscopy (XAS) [14,24,25,39]. To obtain unambiguous results, PES analysis requires the use of clean surfaces due to its high surface

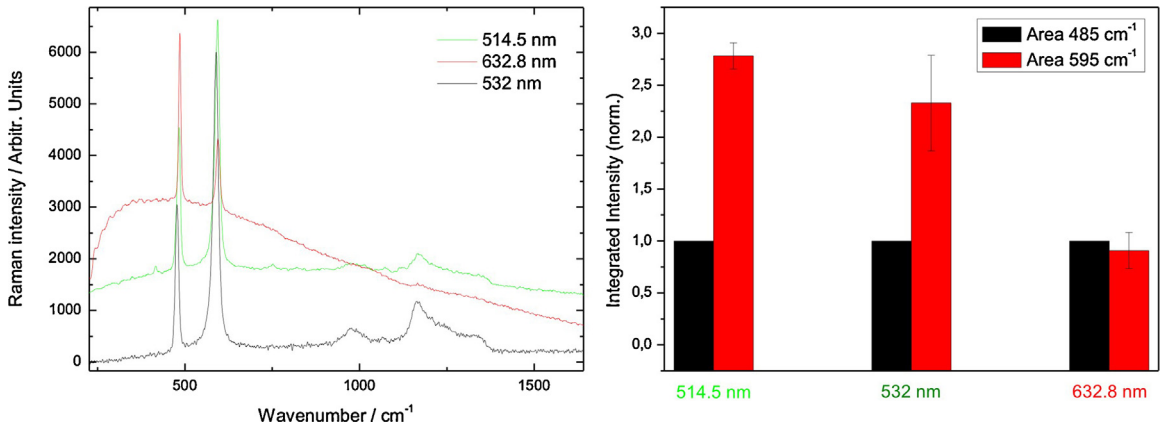

Fig. 7. Left panel: Raman spectra of as prepared $LiCoO_2$ using 514.5 nm, 532 nm and 632.8 nm laser excitation. Right panel: Integrated intensities of the 485 cm^{-1} and the 595 cm^{-1} band after background subtraction for a series of measurements. Reprinted from [34] with permission from Elsevier.

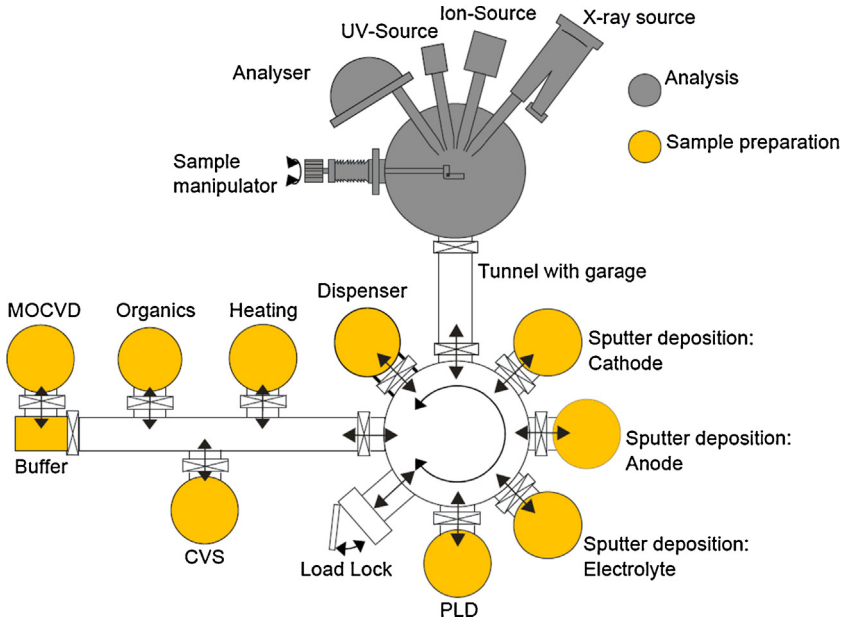

Fig. 8. Illustration of integrated UHV-system for battery research at Darmstadt (Daisy-Bat). The XPS/UPS analysis unit is coupled to several thin film preparation facilities (rf-sputtering, chemical vapor based deposition technologies, pulsed laser deposition) and experimental chambers (*e.g.* for dispensing alkali).

sensitivity. Therefore, the preparation of thin film cathodes, *e.g.* by rf-magnetron sputtering, is a very useful approach (see *e.g.* [40,41]). Several experimental routes can be used to prepare thin film cathodes of different lithiation states (state-of-charge) and to study interface formation with the electrolyte. Prerequisite for a reliable surface science approach is the use of integrated ultra-high vacuum (UHV) systems, featuring both preparation and analysis facilities, to avoid contamination due to ambient air exposure (for an example see Fig. 8). Both synchrotron facilities (*e.g.* solid/liquid analysis system, Solias at Bessy II synchrotron) and laboratory systems are suitable. Use of a synchrotron source is especially attractive due to the measurement of high-intensity, high-resolution Li1*s* spectra and the possibility to tune analysis depth by change of excitation energy. The excitation energy dependence of the photo-ionization cross section can also be used to assign atomic contribution to valence electronic density of states (DOS) by resonance PES [42,43].

To analyze the electronic structure of cathode materials as a function of the lithiation state, two approaches can be followed to adjust the state-of-charge [44], depending on the material: intercalation from the gas phase (for materials prepared in the delithiated state only) [45] and electrochemical (de)lithiation [42,46]. In the first approach, the thin film cathode (*e.g.* TiS_2, V_2O_5) is exposed stepwise to lithium vapor (a dispenser is used as source) and analyzed with PES after each step. The alkali adsorbs from the gas phase, intercalates spontaneously due to chemical potential difference, and diffuses into the film [47]. With exposure time, the lithium content of the film increases at the surface, and gradual lithiation is observed (see Fig. 9). This approach is highly attractive because no side reactions occur and the thin film surface remains clean, ensuring optimal conditions for PES analysis. However, it is restricted to initially lithium-free materials and direct correlation with electrochemical data is excluded.

For electrochemical (de)lithiation by polarization an electrochemical (liquid electrolyte) cell connected to the vacuum system *via* a buffer chamber can be used (Fig. 10). Such a glass cell is operated under protective atmosphere (argon) and features facilities to remove the remaining electrolyte after emersion (rinse and blow-off). In this way it is possible to prepare surfaces without disturbing electrolyte residues and transfer them without contamination to the analysis unit. Similar PES analysis of electrochemical treated electrodes can be found in [14,39,40], but mostly not on thin film electrodes (see *e.g.* [40] for an exception). The approach allows

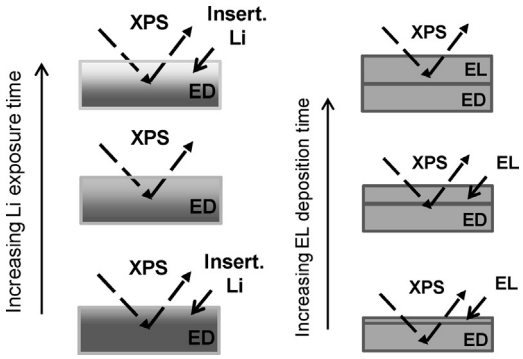

Fig. 9. Illustration of lithium exposure (left) and solid-solid interface experiment (right). A thin film of host material (electrode material, ED) is prepared, exposed to lithium vapor (left) or coated with solid state electrolyte (EL, right), and analyzed by XPS and UPS after each step.

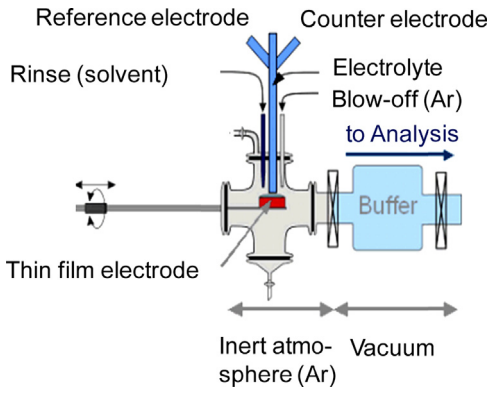

Fig. 10. Schematic sketch of electrochemical cell coupled to UHV-based analysis.

correlation of chemical composition and electronic structure obtained from PES analysis with polarization potential, *i.e.* state-of-charge, and also repeated cycling. However, formation of solid-electrolyte interface (SEI) films may obscure the analysis of the valence band structure, as observed *e.g.* for $LiCoO_2$ and V_2O_5 electrodes. Basically, this limitation may be overcome by the use of an *in situ* all-solid state cell with a cathode top layer, allowing access to PES analysis during operation, *i.e. in operando* (see [48] for sodium intercalation into TiS_2).

The method also allows to investigate the electronic structure of SEI-films. Thin film cathodes need to be cycled in an electrochemical cell [46] or in Swagelok cells first and are then extracted (and transferred) under protective atmosphere prior to analysis [49]. While such procedures allow undisturbed analysis of the films, they do not offer more detailed information about the interface, *e.g.* on electron energy level alignment or double layer. In order to gain more insights into such fundamental properties of the electrochemical interface, additional routes, such as the adsorption of solvent species [50], have to be explored.

For the direct study of interfaces between electrode and electrolyte, interface analysis by deposition of the solid electrolyte onto cathode films with intermediate analysis [51,52] can be performed. In principle also the reverse deposition sequence is possible. This methodology is frequently used to characterize interfaces between electronic materials [53], but was not applied previously to battery interfaces. It gives access to valence band offset, band bending as well as dipole formation at the interface. In such model experiments, interface reaction and related changes in electronic structure can be easily followed. In addition, the shifts of electron chemical potentials as well as electric potential gradients are accessible.

3.4. Modelling of fatigue

As discussed above lithium ion batteries are very complex systems consisting of many components, which can change composition and undergo numerous phase transitions depending on the state of charge and temperature. The transport phenomena and electrochemical states passed through during cycling are determined by gradients in electrostatic potential, concentrations, mechanical strain fields and temperature, which are neither constant in time nor in space. Eventually, this complex system is kept most of its lifetime in a thermodynamically metastable state. All these factors impede the complete physicochemical description of fatigue in lithium ion batteries.

Fatigue is a phenomenon that develops upon electrochemical cycling and over long time scales. Moreover, several of the proposed atomic mechanisms can contribute simultaneously rendering the modelling of fatigue on realistic time and length scales an extremely demanding task. Therefore mainly separate types of models were developed, which can cover restricted length and time scales and provide different levels of detail of the underlying processes. Mathematical and thermodynamic/kinetic models can capture and describe well the evolution of capacity fade or impedance increase in full cells or even stacks [54–56], their disadvantage is that the underlying atomistic processes such as structural changes, phase decomposition, passive layer formation *etc.* remain undisclosed and not accessible. Additionally, transferability and predictive power of those models can be rather poor. In contrast, atomistic modelling can provide a detailed understanding of the fundamental processes leading to battery fatigue and the conditions promoting them. Yet, atomistic simulations are restricted to shorter length and time scales. Among the atomistic simulation methods, electronic structure calculations based on quantum mechanics, such as density functional theory (DFT) calculations [57,58], provide the most detailed information on structural and electronic properties of battery materials and how they change under different physicochemical conditions *e.g.* during cycling. These calculations allow the determination of phase stabilities by comparing total energies of different phases, optimization of crystal and amorphous structures and the investigation of charge densities, electronic band structures or densities of states. Moreover, the availability of parallel computing on large clusters allows studying complex solid-state configurations including point defects (thermodynamic stability and diffusion), thin films and nanostructures. In combination with evolutionary algorithms like USPEX [59,60] or high throughput screening [61,62] DFT calculations allow the prediction of new materials with desired properties [63]. Just recently scientists started to discuss bulk and surface stabilities of cathode materials or their propensity to point defect formation in terms of fatigue evolution. In Section 5, we will give an overview of studies addressing phase stabilities and point defect formation in several cathode materials (mainly $LiCoO_2$) as well as studies on surfaces and electrode/electrolyte interfaces.

4. Effect of structural changes on fatigue: lattice parameters, distortion and cracking

The most important positive electrode materials are layered oxides, derived from $LiCoO_2$, spinels based on $LiMn_2O_4$ and phosphoolivines, represented by $LiFePO_4$. $LiFePO_4$ is considered as the most stable positive electrode material, because both end members, $LiFePO_4$ and fully delithiated $FePO_4$, exist as minerals triphylite and heterosite, respectively. The spinels suffer from a pronounced fatigue in the discharged state at elevated temperature. Responsible is the existence of Mn^{3+}, which disproportionates partially into Mn^{2+} and Mn^{4+}, especially in the surface near regions, where some of the Mn^{2+} is dissolved in the electrolyte and

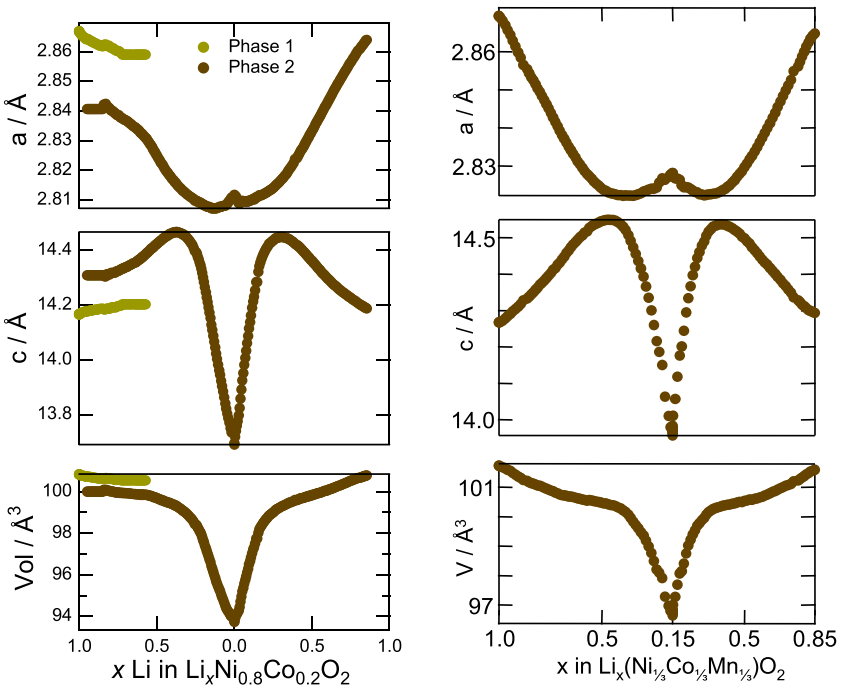

Fig. 11. Evolution of lattice parameters *a* and *c* of $Li_xNi_{0.8}Co_{0.2}O_2$ and NCM.

λ-MnO_2 is formed [64]. $LiCoO_2$ suffers from an intrinsic instability in the delithiated state. At temperatures above 200 °C delithiated Li_xCoO_2 disproportionates into $LiCoO_2$ and "CoO_2", the latter reacts into Co_3O_4 by releasing oxygen [65]. In combination with flammable electrolytes an overheating at high charge levels results in this ongoing exothermal reaction, known as "thermal runaway". Li-occupation levels as low as 40% are observed in commercial $LiCoO_2$-based fatigued batteries [32]. Advanced materials have been derived by replacing some of the Co by other transition metals or Al, like $Li(Ni_{1/3}Co_{1/3}Mn_{1/3})O_2$ (NCM) or $Li(Ni_{0.8}Co_{0.15}Al_{0.05})O_2$ (NCA). These materials are superior to $LiCoO_2$ at least in some of the aspects safety, costs and energy density.

The following considerations are focused on structural aspects of fatigue in layered positive electrode materials, $Li(Ni,Co,Mn)O_2$. The most characteristic feature of structural changes during cycling is the very anisotropic response and the very pronounced extrema at half of the full Li-occupation. This is shown for NCM in Fig. 11 in comparison with LNCO [66].

As lattice parameter *a* is decreasing with Li-extraction and *c* increasing, the *c*/*a*-ratio is a very sensitive parameter to reflect the SOC. The rapid shrinking of the *c*-axis parameter is a consequence of the onset of oxidation of oxygen in agreement with overlapping bands. This results in less repulsion between oxygen layers and shorter distances between these layers. The composition with the maximum in the *c*/*a*-ratio defines a stability limit for the layered oxides as positive electrode materials. Further Li-extraction results not only in an oxidation of a 3*d*-transition metal, but involves also the O2*p*-band (see Figs. 18 and 20). The drastic volume decrease and the very pronounced changes in the *c*/*a*-ratio result in huge mechanical stress, which can cause cracks in the electrode particles. Such cracks appear parallel to each other as seen by Scanning Electron Microscopy (SEM, Fig. 12 left) and Transmission Electron Microscopy (TEM, Fig. 12 right).

Even before cracks appear the mechanical stress leads to lattice distortions and can be measured and quantified by the broadening of the Bragg reflections. This broadening is anisotropic and affects mainly those hkl reflections with high l indices, confirming that the cracks are perpendicular to the *c*-axis. A detailed analysis of half widths and profiles of all reflections in the diffraction patterns reveals two effects on the microstructure, the "platelet" and the "strain" effects [68].

The "platelet" effect describes a very small tilting of less than 1° between nanodomains, resulting in a partial X-ray incoherence (see Fig. 13). This influence on the reflection half widths is described

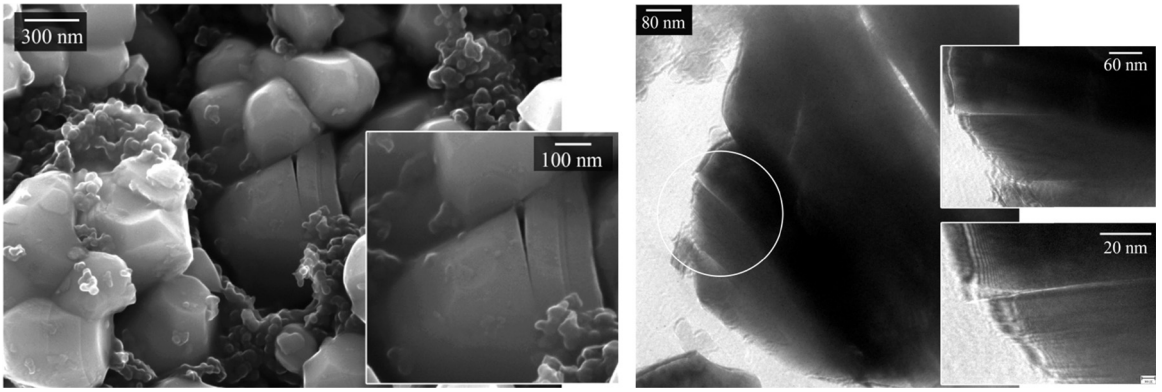

Fig. 12. SEM (left) and TEM (right) images of $Li(Ni_{1/3}Co_{1/3}Mn_{1/3})O_2$ after 10 cycles at C/10 rate in the potential range 3.0–4.2 V *vs.* Li^+/Li in the discharged state. Reprinted from [67] with permission from Elsevier.

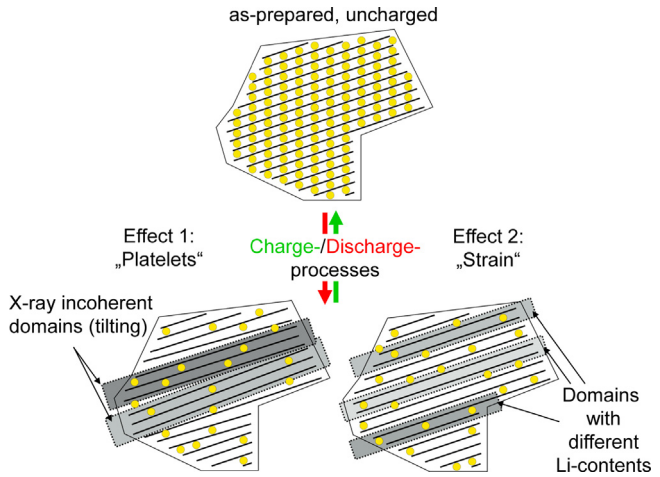

Fig. 13. Schematic representation of two simultaneous effects of cycling on the microstructure. The yellow spheres are Li-ions, arranged in fully occupied layers in the uncharged state. Extraction of Li-ions results in two microstructure effects, described in the text.

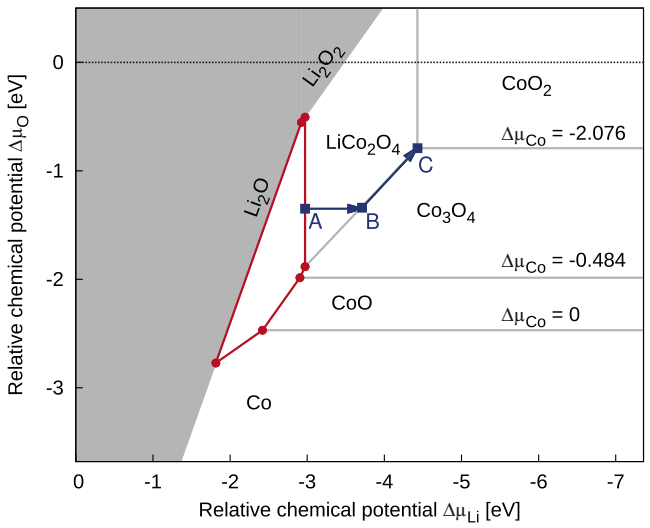

Fig. 14. Grand-canonical phase diagram for the system Li-Co-O. Phase stabilities are given as a function of relative chemical potentials of lithium and oxygen. The stability range of $LiCoO_2$ is indicated by the red polygon.

in detail in literature [69]. A correct description of the observed reflection profiles of partly delithiated layered oxides requires the consideration of a second effect, based on a Gaussian distribution of *c*-parameters and therefore called “strain” effect. The local variation of *c*-axis parameters is not caused by external mechanical stress, but by an inhomogeneous distribution of Li-ions in the layer, resulting in a variation of the interlayer distances. Both microstructure effects are highly reversible, and only some cracks as described above are irreversible and cause a contribution to fatigue.

5. Fatigue and thermodynamics: phase stability, point and planar defects

Standard thermodynamics provide the guidelines for the stability of a material under certain physicochemical boundary conditions. Besides the intrinsic stability of the bulk phase also excess contributions from structural defects such as point defects and surfaces can be described within the framework of equilibrium thermodynamics.

Several degradation mechanisms described in the introduction can be attributed to the intrinsic thermodynamic stability of the anode or cathode material. Firstly, the chemical decomposition of the electrode material into other compounds leads to a mass decrease of active component resulting in capacity fade. Secondly, the formation of point defects on one hand alters the electronic structure and on the other hand reduces the reversibility of lithium intercalation due to structural changes leading to slowing down of charge (ionic and electronic) transport. Finally, morphology changes and decomposition reactions on electrode/electrolyte interfaces can reduce battery performance. In the following it is demonstrated how atomistic simulations can help to understand the underlying processes of these degradation mechanisms and the conditions accelerating them and how the theoretical results correspond to experimental findings.

5.1. Phase stability

During electrochemical cycling undesired side reactions of the active electrode materials can occur leading to dissolution and/or re-precipitation of secondary phases. Such side reactions can be examined theoretically by calculating phase diagrams. Phase diagrams reflect the equilibrium state and do not allow predictions of the accessibility of this state within the time scales of cell cycling and lifetime. Accessing the details of mechanisms of phase transformations by atomistic methods is still challenging. Yet diffusion kinetics of single components can already provide some decisive hints.

For a compound containing several elements the stability range is determined by its own Gibbs free energy of formation and the Gibbs free energies of formation of the competing phases. Thus, stability limits of the chemical potentials for the contained elements can be found, at which the compound can exist as a single-phase or in coexistence with competing phases.

Phase diagrams calculated from *ab initio* can be found in literature for several cathode materials, *e.g.* for the layered transition metal oxides Li_xCoO_2, Li_xNiO_2 and spinel $Li_xMn_2O_4$ [70] or the solid solution $Li_xNi_{1-y}Co_yO_2$ [71] as a function of composition and temperature. An alternative to these canonical phase diagrams are grand canonical phase diagrams, where chemical potentials are used as variables instead of mole fractions (or particle numbers). These allow the examination of phase stabilities depending on the chemical potential of lithium, which can be directly translated into the cell potential of a lithium ion battery.

The stability range of $LiCoO_2$ in relative chemical potential space (*i.e.* chemical potential relative to Li and Co metal or oxygen molecules) is shown in Fig. 14 as a function of lithium and oxygen chemical potentials. This phase diagram was obtained using density functional theory calculations [58,72–74] applying projector augmented plane waves [75,76] with the exchange correlation energy described within the local density approximation (LDA) [77].

$LiCoO_2$ has a very narrow stability range indicated by the red polygon. As soon as the lithium relative chemical potential exceeds −3 eV, $LiCoO_2$ decomposes into other cobalt-rich oxides. The only coexisting elemental phase is cobalt metal. Under lithium rich conditions coexistence with lithium oxide and peroxide are possible depending on the chemical potential of oxygen. The half deintercalated compound monoclinic $Li_{0.5}CoO_2$ is thermodynamically unstable and can therefore not be found in this diagram. According to the simulation, the material is supposed to transform to cubic spinel $LiCo_2O_4$ for $x = 0.5$, which has a large coexistence region with $LiCoO_2$. Cobalt oxide Co_3O_4 possesses a small region of coexistence with $LiCoO_2$ but a large one with $LiCo_2O_4$ at lithium chemical potentials below −3 eV (*i.e.* above +3 eV relative to Li metal), which is important for the deintercalation processes (a possible deintercalation path is indicated by the blue arrows along A-B-C and will

be discussed later). Cobaltous oxide CoO can coexist with $LiCoO_2$ at cobalt rich conditions at relative oxygen chemical potentials between −2 and −2.5 eV. This stability diagram looks very similar to the one calculated by Kramer and Ceder [78]. The main difference is that CoO_2 appears as a thermodynamically stable phase in LDA, while in GGA + U it was unstable against decomposition into Co_3O_4 and molecular oxygen. The thermodynamic stability of layered CoO_2 is subject of an on-going debate although several reports exist on physical properties of this compound [79–81].

Similarly, in the composition dependent (canonical) phase diagram by Wang et al. [70] decomposition of $LiCoO_2$ for different lithium contents was reported. For $0.5 < x < 1.0$ decomposition into layered $LiCoO_2$ and cubic spinel $LiCo_2O_4$ were found and for $x < 0.5$ degradation under oxygen loss into cubic spinel $LiCo_2O_4$ and cobalt oxide Co_3O_4. The cubic spinel was only stable below 270 °C, at higher temperatures it decomposed into layered $LiCoO_2$, cobalt oxide Co_3O_4 and molecular oxygen O_2.

These *ab initio* results reflect exactly experimental findings. Thermal stability of stoichiometric and partly deintercalated Li_xCoO_2 was intensively investigated in the last two decades. Thermal decomposition of Li_xCoO_2 was observed for $x < 0.6$ and the identified secondary phases range from cobalt oxide Co_3O_4 and cubic spinel $LiCo_2O_4$ to cobaltous oxide CoO [65,82–86].

Thus, layered $LiCoO_2$ is thermodynamically unstable also for high lithium content. Still, layered $LiCoO_2$ is metastable enough to become a standard cathode material. The reason why the host structure is maintained over repeated electrochemical cycling is mainly due to kinetic reasons. The above described phase transformations and decomposition reactions require the migration of cobalt (and oxygen) ions. However, the activation energies of cobalt migration in $Li_{0.5}CoO_2$ and CoO_2 were calculated by Reed and Ceder [87]. The authors found that they are reasonably high with 1.6 and 1.9 eV, respectively, which is one order of magnitude higher than the migration barriers reported for lithium ions [88,89]. Hence lithium migration is highly favoured over cobalt migration although it leads to a thermodynamically metastable state. The decomposition processes of Li_xCoO_2 are so slow for $0.5 < x < 1.0$ that they only manifest as fatigue phenomena. Just for $x < 0.5$ the kinetics of phase transformation become reasonably, which is the main reason why in the layered oxides only half of the theoretical capacity is accessible to electrochemical cycling.

5.2. Point defects

During cycling lithium vacancies are created and annihilated in intercalation-type electrode materials. Besides this desired formation of lithium vacancies also other types of intrinsic point defects can occur. Several point defect species have been postulated for $LiCoO_2$ based on experimental results. Oxygen loss leading to oxygen vacancies in the fully deintercalated compound resulting in $CoO_{2-\delta}$ was reported [90,91] as well as formation of peroxide ions O_2^{2-} at high voltages [92]. Moreover, cobalt loss was observed [79,92], the amount of deposited cobalt metal was found to be proportional to the capacity loss of the cell. *Ab initio* calculations support this finding, it was shown that Co^{3+} in $LiCoO_2$ is thermodynamically unstable against reduction to Co metal during cycling [93].

Moreover, it is possible to synthesize over-lithiated Li_xCoO_2 with $1.0 < x < 1.15$ [94], although these solid solution compounds are thermodynamically not stable [95]. The excess lithium is assumed to replace cobalt resulting in anti-sites Li''_{Co} with charge compensation by oxygen vacancies $V_O^{\bullet\bullet}$ [95,96]. Oxygen treatment removes oxygen vacancies from the lattice and improves capacity reversibility [94].

Anti-site formation is a well-known problem in layered $LiNiO_2$, which is almost impossible to be synthesized in a stoichiometric ordered way, but results as $Li_{1-d}Ni_{1+d}O_2$.

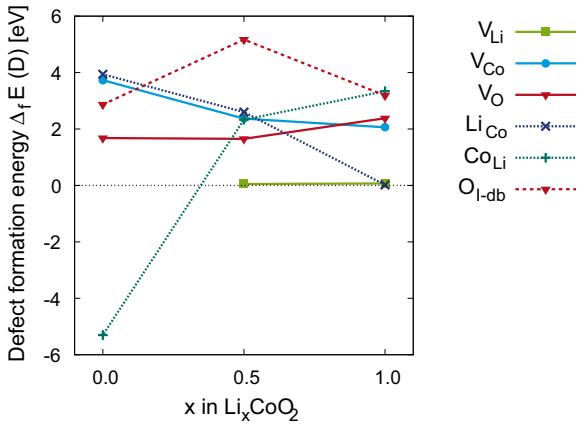

Fig. 15. Defect formation energies calculated for the compounds $LiCoO_2$, $Li_{0.5}CoO_2$ and CoO_2 to mimic the deintercalation process. Chemical potentials correspond to points A, B and C in the phase diagram.

For semiconductors the study of the thermodynamic stability limits and of formation energies of point defects depending on chemical potentials of atoms and electrons is already a standard routine [97,98]. However, to battery materials this technique has not been applied until very recently [99–102]. Within this formalism formation energies are calculated for single defects (not pairs, such as Frenkel or Schottky defects) with respect to thermodynamic reservoirs represented by their chemical potentials, according to

$$\Delta_f E(D^q) = (E_{\text{Defective}} - E_{\text{Host}}) + q(E_{\text{VBM}} + E_{\text{F}}) - \sum_i \Delta n_i \mu_i \qquad (4)$$

where $E_{\text{Defective}}$ is the total energy of the defective system, E_{Host} is the total energy of the perfect reference, q is the charge state of the defect, E_{VBM} is the position of the valence band maximum and E_{F} the Fermi energy, Δn_i denotes the number of atoms of type i exchanged in the defective system, and μ_i is the chemical potential of the reference phase (thermodynamic reservoir) of atom type i.

Defect formation energies are related directly to the temperature dependence of defect concentration, which is given by

$$c(D^q) = c_i^0 \exp\left(-\frac{\Delta_f E(D^q)}{k_B T}\right) \qquad (5)$$

where c_i^0 denotes the concentration of available lattice sites for the respective defects.

Only few studies exist so far on intrinsic point defects in stoichiometric $LiCoO_2$ using *ab initio* calculations [100–102]. Takamatsu et al. found that under lithium-rich conditions (coexistence with Li_2O) at oxygen chemical potential of −1 eV or less $LiCoO_2$ was no longer stable due to massive cobalt anti-site formation $Co_{Li}^{\bullet}$ compensated by Co^{2+} on a regular lattice site (Co'_{Co}). The authors suggest this reaction to be responsible for the surface reduction of Co species in presence of electrolyte as observed by XANES [100]. Similarly, in the work of Koyama et al. $Co_{Li}^{\bullet}$ anti-sites, besides oxygen vacancies $V_O^{\times}$ and lithium interstitials $Li_I^{\bullet}$, are reported to be the dominating point defects both at synthesis conditions (coexistence with Li_2O, high oxygen partial pressure) and under reducing conditions as they can be found inside the battery (very low oxygen partial pressure).

$LiCoO_2$ is known to be a p-type semiconductor [103], which is reflected in its propensity to formation of negatively charged lithium vacancies V'_{Li} compensated by holes $h^{\bullet}$. In Fig. 15 defect formation energies of the defects with lowest formation energies are shown (interstitials of Li and Co have higher energies than presented) for the compounds: $LiCoO_2$ ($x = 1$), monoclinic $Li_{0.5}CoO_2$ ($x = 0.5$) and CoO_2 ($x = 0$). The chemical potential conditions for

$x = 1.0$, 0.5 and 0.0 correspond to the chemical potentials in points A, B and C, respectively. Therefore, the chemical potentials in A and C reflect equilibrium conditions of layered $LiCoO_2$ and CoO_2, respectively, while B was chosen as a possible path from A to C, as $Li_{0.5}CoO_2$ is a metastable phase.

Given are the energies of the charge states for Fermi energies about 0.2 eV above the valence band maximum in layered $LiCoO_2$. For the metallic compounds $Li_{0.5}CoO_2$ and CoO_2 only neutral defects need to be considered. The stoichiometric material is at the chosen conditions not only prone to the desired lithium vacancies V'_{Li} but also to Li anti-sites Li''_{Co} and cobalt vacancies V'''_{Co}. Cobalt can dissolve into the electrolyte and migrate to the anode, while lithium ions occupy its free crystal sites. Depending on the activation barrier from the anti-site back into the regular lithium sub-lattice position these lithium ions can be trapped and do not contribute to electrochemical cycling anymore.

At $x = 0.5$, another dominating defect can be observed: the oxygen vacancy $V^{\times}_{O}$, which leads to oxygen loss of the sample.

When the lithium content is decreased below $x < 0.5$ the cobalt anti-site formation becomes crucial *i.e.* it possesses even a negative formation energy, which can be understood as equivalent to the decomposition into the spinel and rock-salt compounds. Thus, lithium contents of $x < 0.5$ lead to serious disintegration of the cathode material and have to be definitely avoided.

Oxygen interstitials in the dumbbell configuration, which can lead to peroxide $O^{\times}_{I-db}$ or superoxide $O^{\bullet}_{I-db}$ ions, have high formation energies and seem favourable only below $x < 0.5$.

There exist few more studies on point defects in other cathode materials. Kim investigated the influence of Co substitution on vacancy formation energies in $LiNiO_2$, but did not take into account chemical potentials of the reservoirs for elements and charge carriers [71]. The only elaborate study in the full spirit of semiconductor defect thermodynamics can be found for $LiFePO_4$ by Hoang and Johannes [99]. The authors not only calculated defect formation energies taking into account the thermodynamic limits of the host material but also provide insights into charge transport mechanisms.

5.3. Planar defects

Other important fatigue mechanisms can be traced back to changes of surfaces and interfaces like surface reconstructions and/or changes of particle morphologies during cycling, as surface chemistry depends severely on surface orientation. Both processes alter the charge transport properties of the electrode/electrolyte interfaces. This is even more important as most electrode materials exhibit highly anisotropic diffusion paths ($LiFePO_4$: 1D, graphite and layered TM oxides: 2D, spinels: 3D). As a result not all surfaces are penetrable for Li ions, thus charge transport is blocked in certain directions.

Equilibrium crystallite shapes depend on environment (*e.g.* reducing or oxidizing conditions) and can therefore change from component fabrication (*e.g.* annealing at elevated temperatures) to assembly of the battery stack leading to surface growth and shrinkage of electrode particles in contact with the reducing electrolyte, and even during cycling. Another issue related to surfaces are grain boundaries and their stability and transport properties.

The equilibrium morphology of a crystal can be determined from surface energies and the Wulff construction. This was done for almost all simple cathode materials so far ($LiFePO_4$ [104], $LiCoO_2$ [78,105], $LiNiO_2$ [105], $LiMn_2O_4$ [106,107]). Kramer et al. studied the morphology of $LiCoO_2$ crystals depending on the chemical environment [78]. The authors found that different surfaces are stable under reducing and oxidizing conditions. While under oxidizing conditions hexagonal shaped crystallites with large portion of (0 0 0 1) facets (impenetrable for Li ions) result, reducing conditions favour (10–14) facets, which should offer higher rate capabilities. Kim compared the morphologies of $LiCoO_2$ and $LiNiO_2$ [105]. Surface energies of $LiNiO_2$ were found to be lower than of $LiCoO_2$, due to the reduced covalence of the TM-O bonds in $LiNiO_2$, as the number of broken TM-O bonds mainly determines the surface energy.

Surface reconstruction is primarily an issue in spinel $LiMn_2O_4$. Benedek and Karim both found that the (1 1 1) surface can only be stabilized after surface reconstruction. Karim found the (1 1 1) surface to be the most stable with an inverse spinel structure in the topmost layers, *i.e.* Li and Mn exchange sites resulting in terminal Li ions [107], while Benedek reports stoichiometric top layers after reconstruction, but (0 0 1) surface still lead to lower energy [106]. The average oxidation state of Mn was found to be reduced compared to the bulk, some ions were even found to be in a divalent state, which probably favours dissolution and irrecoverable loss of manganese.

It is well known that not only surface energies determine the final crystal shape but also surface stresses need to be taken into account [108], which should be integrated into future studies.

Real surfaces and the effect of Li/vacancy ordering at the surface of $LiCoO_2$ was investigated using a combination of STM experiment and *ab initio* calculations by Iwaya et al. [109]. Moriwake studied Li diffusion along a coherent grain boundary and due to domain formation in thin films of $LiCoO_2$ [110,111].

Towards modelling fatigue mechanisms it is indispensable to study not only clean and ideal surfaces, but also the stability and properties of interfaces between electrode materials and other components such as electrolyte, carbon black, binder and decomposition products. The studies of interactions between electrode material and electrolyte are primarily focusing on the SEI formation and its properties on the graphite anode so far [112–118].

The formation of an SEI on graphite anodes was first studied using a kinetic Monte Carlo algorithm by Methekar to investigate growth during the first cycles and time evolution of the passivation layer [112]. The later studies made use of *ab initio* molecular dynamics (AIMD) simulations, which allow investigation of redox processes between the surface of graphite and the molecules of the liquid electrolyte [113] including the effects of other components like Li salts [118]. Leung developed a framework that allows to study the voltage dependence of those processes [115] and investigated also ethylene carbonate decomposition on $LiMn_2O_4$ surfaces [114].

6. Electronic processes: electronic structure of bulk materials and interfaces

Since the advent of the rechargeable Li-ion batteries in 1991, the electronic structure of layered cathode materials has been extensively studied theoretically and experimentally (see *e.g.* [119–122]). This section focuses on the *in situ* PES and XAS studies of the electronic properties of thin film cathode materials and their interfaces to elucidate the stability *vs.* potential. Such an approach has a great advantage that electronic and crystallographic structures are not affected by impurities, allowing direct assignment of experimentally obtained results with *ab initio* calculated electronic properties of the material.

6.1. Bulk properties and Fermi level

Oxide cathode materials are ionic transition metal compounds with significant covalent character [123]. Their basic electronic structure is determined largely by the Madelung potential and the perturbation of the crystal field around the TM-ions resulting in splitting of the *d*-electron levels [4,123,124]. Covalent interaction

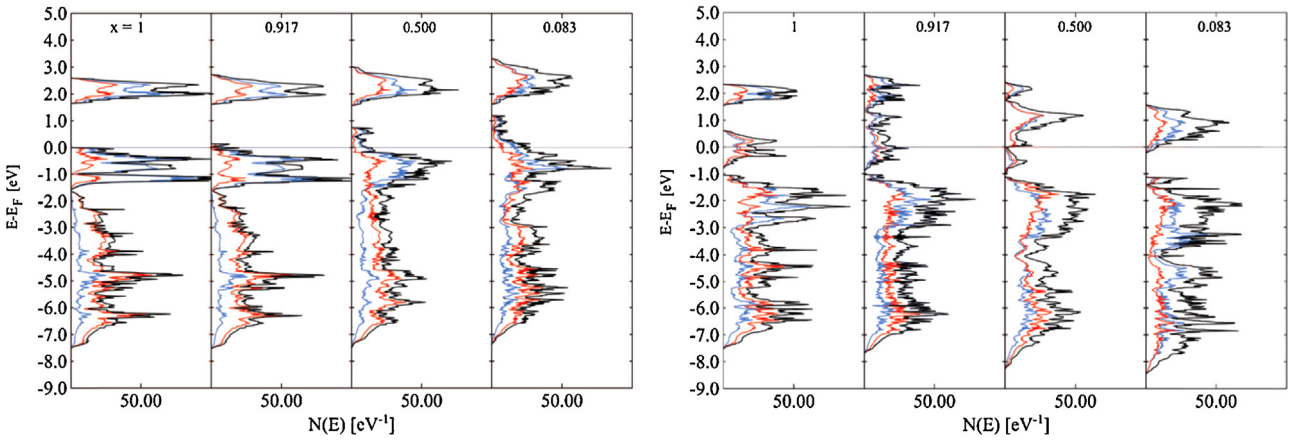

Fig. 16. DOS (black curves) and PDOS for Co and Ni (blue curves) and O (red curves) for different values of x in Li_xCoO_2 (left) and Li_xNiO_2 (right); ($E_F = 0$). Reproduced from [46] with the permission of the PCCP Owner Societies.

of the (non-bonding) *d*-electrons with the oxygen coordination shell results in hybridization and energy bands of different bonding characters [5], with far-reaching consequences for the electronic conductivity and stability of the compounds. Theoretical considerations concerning the band structure and experimental observations regarding the decomposition potentials of various cathode materials lead to the concept of intrinsic voltage limit, which describes charge compensation and electrode potential by operation of a redox couple in the framework of solid state chemistry [5]. In the fully lithiated (or discharged) state, the $(d+p)^n/d^{n+1}$ redox couple of primarily cation *d*-character is located above the anion *p*-band and clearly separated. Upon deintercalation, *i.e.* polarization to more positive potentials, the distance between the redox couple and the anion *p*-band decreases. At the intrinsic voltage limit, the $(d+p)^n/d^{n+1}$ redox couple of primarily cation *d*-character crosses the top of the anion *p*-band and changes to primarily anion *p*-character. Upon further deintercalation, the redox couple falls further below the top of the anion *p*-band and holes form in the bonding anion *p*-states, resulting in anion oxidation, *i.e.* decomposition by oxygen loss (see also [125]).

Fig. 16 shows densities of states (DOS) obtained from DFT calculations performed for Li_xCoO_2 and Li_xNiO_2 as a function of lithium content *x*. The contribution of the atomic partial density of states (PDOS) to the overall DOS is shown by the colour code. For $LiCoO_2$, valence band states of predominantly Co3*d* character are involved in initial charge compensation ($x > 0.5$). For smaller *x* also O2*p* states are involved, due to changes in the DOS with lithium deintercalation resulting in increased hybridization of Co3*d*/O2*p* valence band states.

In Fig. 17, PES and XAS analyses of a $LiCoO_2$ thin film electrode are shown. The valence band (VB) structure of $LiCoO_2$ in the upper-valence-band region (1–3 eV, Fig. 17, left), is dominated by the Co3*d*

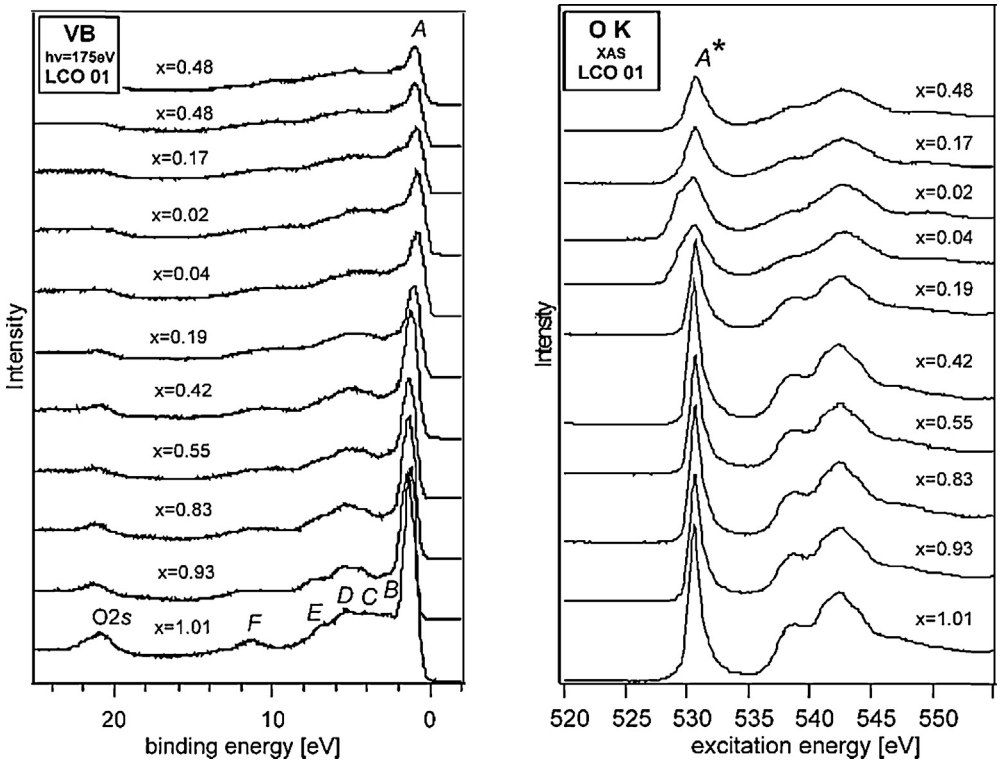

Fig. 17. The density of the occupied (left) and unoccupied (right) electronic states *vs.* the electrode potential of a Li_xCoO_2-film as the experimentally obtained from photoemission of the valence band structure and O *K* XANES, respectively [126].

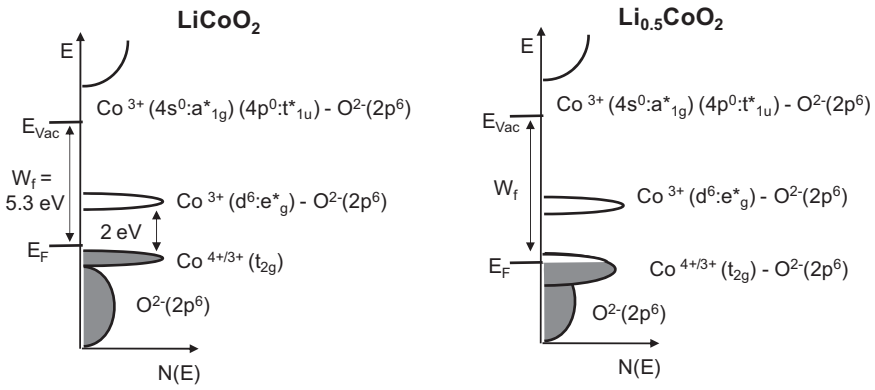

Fig. 18. Electronic band structure of $LiCoO_2$ (left) and $Li_{0.5}CoO_2$ (right) as deduced from DFT calculations and PES/XAS measurements.

emission, whereas the region between 3 and 10 eV corresponds to O2*p* and O2*p*/Co3*d*-like contributions. A Co3*d* final state satellite is situated at about 12 eV. The shape of the O K-edge of a stoichiometric Li_xCoO_2 film (Fig. 17, right) indicates explicitly a low-spin configuration of Co^{3+} ions (t^6_{2g}, $^1A_{1g}$) under octahedral (O_h) symmetry. The sharp line A^* at 530.6 eV corresponds to transitions of an O1*s* electron into unoccupied Co3*d*(e_g)-O2*p* hybridized states. The structures above 535 eV have been attributed to transitions into Co4*s* and 4*p*-derived states with O2*p* admixtures [42].

Upon lithium deintercalation the Fermi level (E_F) shifts into the Co3*d*(t_{2g}) states and the Co3*d*(t_{2g}) states become broader (Fig. 17, left), while the Co3*d*(e_g)-O2*p* hybridized unoccupied states are not influenced by lithium removal up to the potential of 4.2 V in the experiment (Fig. 17, right). Therefore, the charge compensation takes place first at the Co site. However, a drastic change of the feature A* in XAS occurs when lithium is removed further (4.3 V and above). The Fermi level E_F reaches a critical value when the Co3*d* states ($Co^{4+/3+}$ couple) cross the top of O2*p* bands, which is accompanied by a hole transfer to the O2*p* states. The removal of a significant amount of electrons from the O2*p* band results in oxidation of O^{2-} and oxygen loss from the lattice leading to degradation of the cathode material. Thus, the proximity in energy of t_{2g} and O2*p* bands determines the intrinsic voltage limit [5,126] for the $LiCoO_2$ cathode material. The experimental data are in good agreement with the DFT calculations as discussed in detail in [46]. The changes within the structure and occupation of the DOS during deintercalation are schematically summarized in Fig. 18.

The synthesis of stoichiometric $LiNiO_2$ with low-spin (LS) Ni^{3+} ($t_{2g}^6e_g^1$) electronic configuration is still a challenge. Comparative studies of the temperature stability of $LiCoO_2$, $LiNiO_2$ and $Li(Ni,Co)O_2$ thin film cathode materials have shown that the Ni^{3+} ($t_{2g}^6e_g^1$) with LS state is less stable than the Co^{3+} ($t_{2g}^6e_g^0$) with LS state [127]. Temperatures which are optimal for the film growth of stoichiometric $LiCoO_2$ are not sufficient for proper crystallization of $LiNiO_2$ and $Li(Ni,Co)O_2$ films [128], whereas higher temperatures lead to simultaneous reduction of Ni^{3+} ions to the high spin (HS) Ni^{2+} ($t_{2g}^6e_g^2$) state and Li-loss from the sample.

Instead of thin films based on pure $LiNiO_2$ thin films based on the mixed oxide $Li(Ni,Co)O_2$ can be investigated. Similar to $LiCoO_2$, the electron density of the occupied states of a stoichiometric $LiNiO_2$ ($Li(Ni,Co)O_2$) film is dominated by the Ni3*d* state (Ni3*d*/Co3*d*) (1–3 eV of the VB structure in Fig. 19, left); the region at 3–9 eV belongs to the O2*p* states and the Ni3*d*-O2*p* (Ni3*d*/Co3*d*-O2*p*) hybridized valence band states (Figs. 16, right and 19, left). The unoccupied Ni3*d*-O2*p* hybridized states of a $LiNiO_2$ film cathode material are influenced by the Li^+ deintercalation (Fig. 19, right), but the Fermi level remains located in the antibonding states and does not cross the occupied O2*p* states of $LiNiO_2$ (see Fig. 20 for illustration).

These results elucidate that the charge compensation occurs mostly on the antibonding states at the Ni-site of $LiNiO_2$. Therefore, the nickel based compounds have a higher intrinsic voltage limit, *i.e.* are more stable with respect to charge compensation upon Li-ion removal.

These findings demonstrate that the electronic structure of the layered oxide materials changes substantially upon deintercalation, and that oxidative decomposition is triggered by the formation of holes in binding O2*p* dominated valence band states. Oxygen loss corresponds to the formation of oxygen vacancies, indicating the tendency of the material to compensate for the removal of lithium by formation oxygen vacancies at low lithium content. Considering the metastable character of partially deintercalated Li_xCoO_2, as indicated by phase diagram calculations and evidenced by thermal decomposition, the major impact of hole formation will be an increase of decomposition kinetics.

The investigations on the electronic structure of layered cathode materials highlight the significance of the (partially) covalent character of the TM—O bond for stability. Removal of electrons upon delithiation from states with strong (bonding) covalent character (strong O2p admixture) results in oxygen loss and is to be avoided. On the other hand, covalent interaction may be beneficial in the case that electronic states with antibonding character are involved, and can thus be used to design cathode materials with higher stability at low lithium content, *i.e.* higher capacity, considering especially the dependence of TM-anion covalency on element electronegativities and bond length [5,123]. Operated under conditions that normally ensure capacity reserve to counteract overcharge, cathode materials with higher reversible capacities may also be used to prolong life time.

6.2. Interface reactivity and energy level alignment

Real Li-ion battery electrodes possess various interfaces, from which the interface between active material and electrolyte is the most important one. This interface is characterized by the Li-ion transfer and (near) electrochemical equilibrium conditions for Li-ions (see *e.g.* [16]), dominating the electric potential gradient at the interface with significant impact on the overall electrode potential. Other ions than Li-ions, as well as electrons, are usually far from equilibrium at this interface, resulting in a driving force for dissolution, electrolyte decomposition and surface layer formation. The perception that these processes at the cathode/electrolyte interface are relevant to cell fatigue initiated increased activities over the past years to analyze surface layers on cathodes. In contrast to the SEI formed on the graphite anode, cathode materials develop thin and laterally inhomogeneous surface films, which are composed of different layers [14]. An inorganic surface layer forms due to cathode surface deterioration

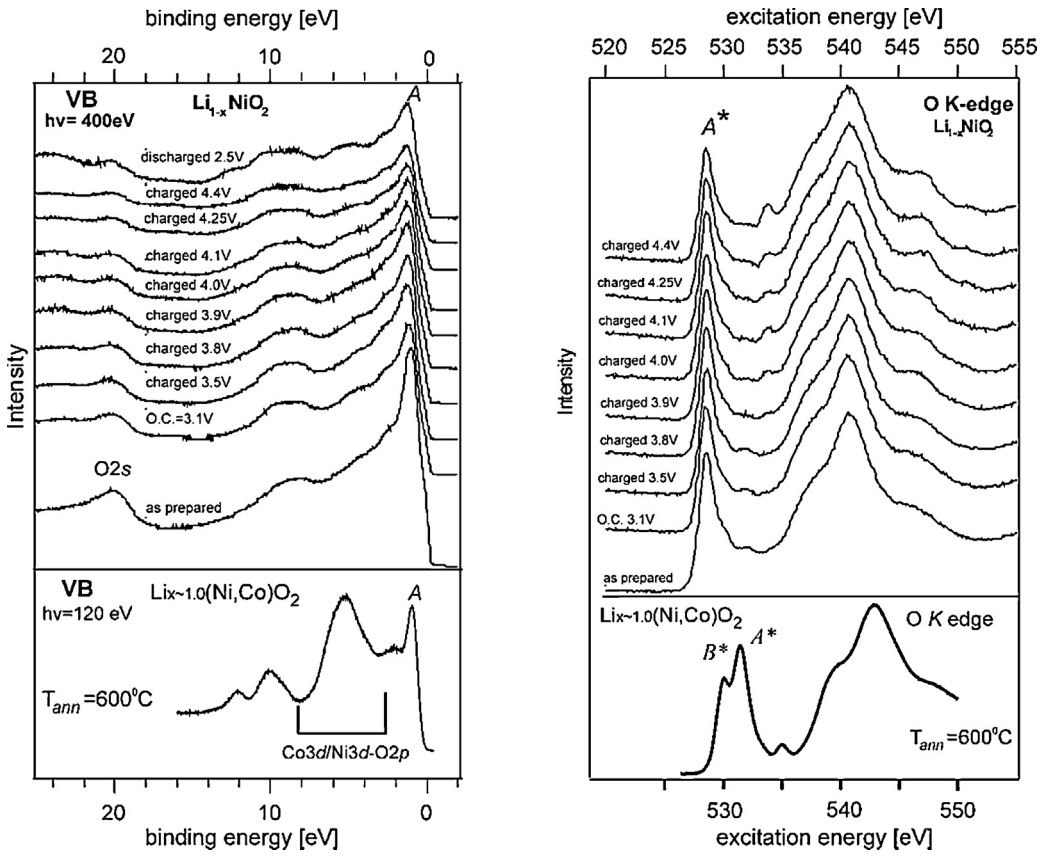

Fig. 19. The density of the occupied (left) and unoccupied (right) electronic states *vs.* the electrode potential of a Li_xNiO_2-film (the upper plots) and of a stoichiometric $Li(Ni,Co)O_2$ film [129] as experimentally obtained from photoemission of the valence band structure and O *K* XANES, respectively. The spectral features *A** and *B** of the LNCO film are contributed from unoccupied Ni^{3+} 3*d*(e_g)-O2*p* and Co^{3+} 3*d*(e_g)-O2*p* hybrid states, respectively [129].

such as surface reconstruction or phase change [25], covered by a layer of organic and inorganic compounds from electrolyte decomposition. Important key concepts for initial reactions are electrode-surface induced decomposition of electrolyte species [23], oxidation of electrolyte species at high electrode potentials [5], and the related reduction of electrode-surface transition metal ions [100], resulting in transition metal dissolution and phase change [14,23,130,131]. To counteract interfacial processes and increase the stability of the cathode, thin protective coatings (*e.g.* ZrO_2, Al_2O_3, LiPON, LiF) have been applied (see *e.g.* [132–134]).

Of crucial importance for the stability of the electrolyte in contact with the electrodes is the electrochemical stability window of the electrolyte [4]. Electrodes operated outside this window induce electrochemical electrolyte decomposition. Specifically, electrolyte oxidation occurs when the electrode Fermi level, *i.e.* the electrochemical potential of the electrons within the electrode, is located below the electrolyte HOMO level [5,123] (see Fig. 3). Some data suggest that the oxidative stability of solvents and salts typically used for Li-ion liquid electrolytes are quite high, *i.e.* in the range of 6.2–6.7 V *vs.* Li/Li^+ for carbonate based solvents and 3.0–3.8 V *vs.* SCE (aqueous standard calomel electrode) for salts [6]. However, it is well known that the onset of oxidation of typical electrolytes is below 4 V *vs.* Li/Li^+ (see *e.g.* [135]), and that the electrolyte participates in the formation of the SEI-layer [14]. This discrepancy

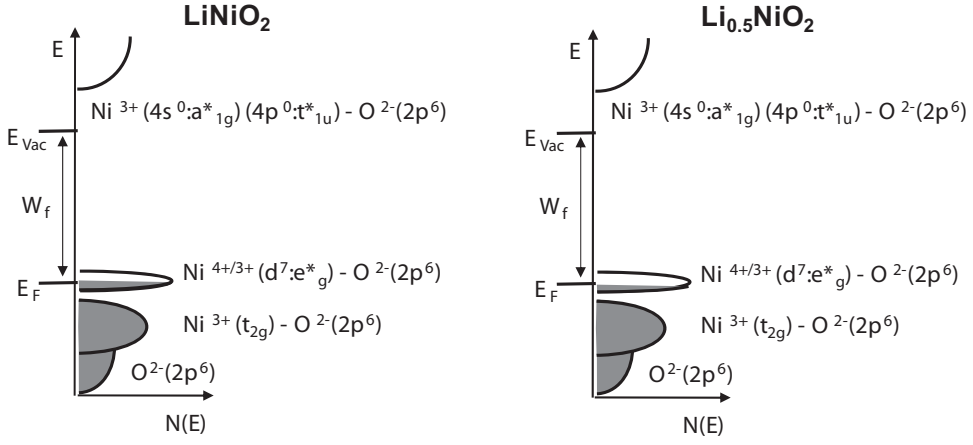

Fig. 20. Electronic band structure of $LiNiO_2$ (left) and $Li_{0.5}NiO_2$ (right) as deduced from DFT calculations and PES/XAS measurements.

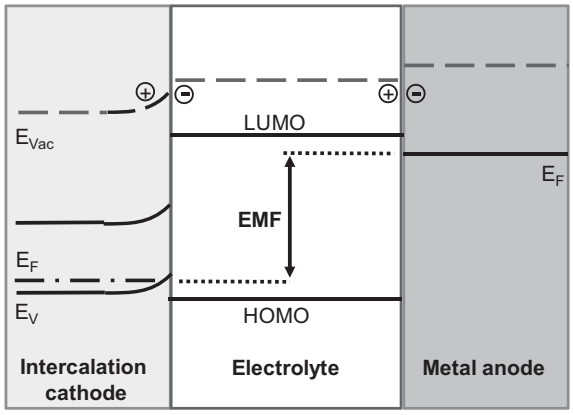

Fig. 21. Schematic illustration of an electronic energy level diagram of a lithium cell.

is likely due to differences in surface chemistry and double layer formation for the various electrode materials.

Surprisingly, not much attention has been paid in the past to the electric potential gradient at the interface, although it is known that double (dipole) layers can have significant impact on energy level (mis)alignment [136,137]. Additionally, for ionic phases with low charge carrier concentrations diffuse charged layers (space charge layers) are encountered at interfaces [15], which induce band bending and related charge carrier concentration changes with significant impact on the charge transfer rate and interface stability [136]. In fact, electronic energy level diagrams of Li-ion cells have essentially remained conceptual in nature without the detailed and experimental-based input about the electric (contact) potential distribution required to assess charge transfer phenomena, defect formation at interfaces and interface layer stability in real systems (see Fig. 21 for an energy level diagram including electric potential gradients at the interfaces). Also, such electronic energy level diagrams have not been combined with corresponding ionic level diagrams [16], as is conceptually possible and is demonstrated later in this section.

A rigorous chemical analysis of the SEI-layer on cathodes requires the use of thin film cathodes and of an appropriate electrochemical cell coupled to the XPS analysis unit. The major benefit of such an approach is that the absence of carbon-black and binder, present in composite electrodes. This leads to increased sensitivity of the measurement towards SEI-related carbon and fluorine species and allows unambiguous identification of the observed reaction products formed on the surface of the active cathode material. The pristine surface is also free from any reaction products resulting from contact with the ambient air, in contrast to commercial cathode powder, where reaction products such as lithium carbonate cover the surface before contact with the electrolyte. Clearly, such initial surface layers should influence the reactivity of the electrode surface with the electrolyte. Notably, in $LiPF_6$ containing electrolytes, the initial surface layer undergoes reaction due to the presence of HF, *i.e.* lithium carbonate is dissolved [4].

If immersion and initial cycling of $LiMO_2$ thin film electrodes is conducted in carbonate-based (PC, DMC) electrolytes with lithium salts with and without fluorine ($LiPF_6$, $LiClO_4$), the formation of a very thin surface layer containing lithium oxide, lithium carbonate, polymeric carbon compounds can be observed (as well as fluoride-containing compounds, when $LiPF_6$ is used as salt), see Fig. 22. These findings are qualitatively comparable to results obtained on cycled composite electrodes [14,49,138]. However, a significantly lower fraction of carbon components at high binding energy, usually attributed to the presence of polycarbonates [14], is observed compared to the cycled composite electrodes. This probably reflects the initial character of the surface layer formation in the thin film

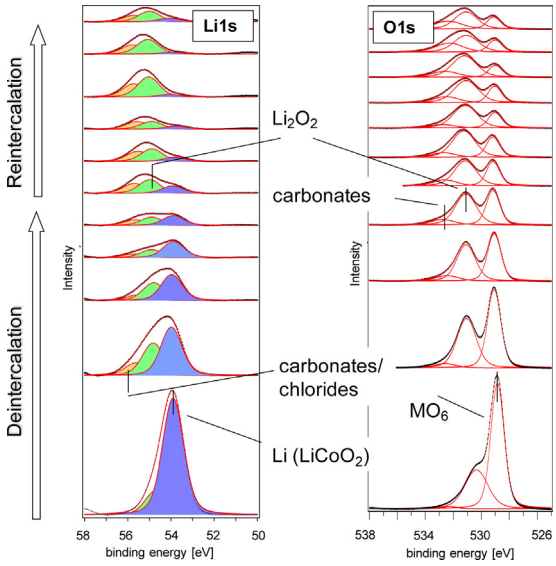

Fig. 22. Surface film formation on $LiCoO_2$ thin film electrode after electrochemical deintercalation and (re)intercalation in a PC/$LiClO_4$ electrolyte, as evidenced by the Li1*s* and O1*s* XPS core level spectra.

experiments, and indicates that polycarbonates are formed only later at higher cycle numbers. Possible other reasons are different initial surface chemistry and lower amount of HF due to the absence of PVDF-binder. Further investigations are required to elucidate this issue.

Polarization or cycling of $LiCoO_2$ thin film electrodes however results in the presence of a reduced surface layer (reduced cobalt ions (Co^{2+}), oxygen loss), as generally observed also for $LiMO_2$ composite electrodes [23,25,100,139].

The stability of electrodes with respect to contact with electrolyte may be investigated by low temperature adsorption on thin film electrodes. These experiments allow also fundamental insights into cathode/electrolyte interface interaction and electrochemical interface formation. Such adsorption experiments were performed with alkyl carbonate solvent (DEC, DMC) on $LiCoO_2$ cathodes [140–142]. Adsorption experiments with ionic substrates have hardly been conducted in the past, even if dedicated surface analysis, partly also on thin film electrodes, is performed rather frequently [24,25,41,100,143,144]. Although adsorption experiments have mainly model character, they resemble the situation during composite electrode fabrication, when the active cathode material is brought in contact with a solution of low ion concentration.

Upon adsorption of DEC onto clean, freshly prepared $LiCoO_2$ a small amount of chemisorbed (or decomposed) organic species are detected next to physisorbed DEC. No changes in the cobalt signals (Co2*p*, Co3*p*) are observed, demonstrating that no significant reduction of cobalt (Co^{3+} to Co^{2+}) takes place. This indicates also the absence of DEC oxidation (*i.e.* negligible hole transfer from $LiCoO_2$ to DEC) and of the formation of a reactive chemical layer involving the cathode surface. The position of the HOMO level of the adsorbate phase, extracted from valence band spectra, is *ca.* 4 eV below the $LiCoO_2$ valence band maximum, rendering hole transfer extremely unlikely. Despite these facts, it can be found that the presence of the adsorbate phase leads to pronounced downward band bending (up to 0.8 eV) and to a decrease of the work function. This originates from Li-ion transfer to the adsorbate phase, as indicated also by the spectral features of the Li1*s* signal. If DMC is used as adsorbate phase, a higher reactivity and less band bending is observed.

Fig. 23 shows the energy level diagram for the $LiCoO_2$/DEC interface, reflecting the formation of the electrochemical double layer.

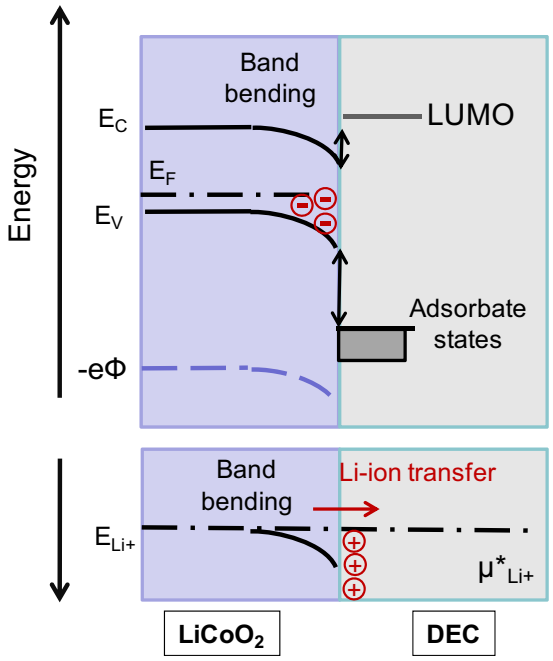

Fig. 23. Electron and ion energy level diagram of the $LiCoO_2$/DEC interface established from low temperature adsorption of DEC. Note that the Li-ion levels are deduced from theoretical considerations. Reprinted with permission from [141]. Copyright 2014 American Chemical Society.

It is expected that charge transfer is dominated by the transfer of Li-ions in order to align the ionic electrochemical potential of Li^+ in the two phases (the chemical potential of Li-ion is initially very low in the DEC adsorbate phase). Note that the position of the electron energy levels can be extracted from experimental data, while the position of the ion energy level cannot. However, from theoretical considerations it is quite clear that (1) the Li-ion energy level is bent in the opposite direction than the electron energy levels, due to the opposite charge of the ion, (2) in the bulk the chemical potential of the Li-ions should be close to the energy level corresponding to vacancy-doped (*i.e. p*-doped) $LiCoO_2$ and (3) electron and Li-ion chemical potential should amount to the lithium chemical potential (see *e.g.* [145]). With such energy level diagrams, the interface is widely characterized also with respect to its kinetic properties, as it contains energy level off-sets as well as any charge carrier concentration changes, as evidenced by band bending.

As expected, fully intercalated $LiCoO_2$ behaves like a semiconductor. High electric gradients in the surface region are expected to have a significant impact on the transport of charged defects, potentially supporting degradation by defect migration, *e.g.* related to TM-ions (see [146]). The adsorption experiments though show that the $LiCoO_2$/DEC interface is basically non-reactive, indicating that salt and/or Li-deintercalation is required to trigger pronounced reactivity.

7. Degradation phenomena on cell level: SEI formation, cathode overcharge and composite electrode effects

The important performance parameters of electrochemical energy storage devices, like energy and power densities, safety and lifetime aspects or cost issues are only defined on the full cell level. A systematic investigation of the lifetime of a Li-ion battery must therefore consider all possible degradation mechanisms, from the possible corrosion of current collectors, changes in the bulk electrode materials, interface reactions between electrodes and electrolyte, oxidation and reduction of electrolyte components or blocking of Li-ion transport through the separator. Most of these effects lead to increasing transport barriers.

A serious safety risk is the formation of Li-dendrites on the negative electrode side, which can penetrate the separator and cause a short-circuit [147]. The proceedings of the specific side reactions, which are responsible for fatigue, depend strongly on the operation conditions and the full history of the device. A stable anodic solid electrolyte interphase (SEI) developed during initial formation of the cell is a necessary precondition for a good life time of a cell. A too thick SEI, however, hinders Li-ion transfer, increases internal resistance and reduces the overall performance. The appropriate choice of electrolyte components is of primary importance for the formation of the SEI, very often supported by dedicated additives to tailor the properties of the SEI. Most of the Li-ions, which are chemically bound in the SEI come from the positive electrode material and are directly responsible for a significant irreversible capacity loss in the first cycle. The negative electrode is always slightly overbalanced, meaning that more active electrode material is used on the negative side than actually needed to match the capacity of the positive electrode during normal operation. These additional vacant sites for Li-intercalation into graphite should minimize the risk of competing Li-dendrite formation on the graphite or SEI surface. The capacity of the cell is therefore limited by the available Li-ions from the positive electrode, so that any loss of Li during formation causes directly a capacity loss. Overbalancing is a cell design tool to enhance safety at the cost of energy density on cell level.

Fatigue on cell level must be studied over about 1000 cycles. Therefore, the investigation of very good materials requires the use of commercial-type cells without any artificial degradation caused by imperfections in cell manufacturing. Cylindrical 18650-type cells are excellent objects for investigations with neutrons and high-energy photons and were studied comprehensively [148,149]. The potential of these *in operando* studies is by far not exploited yet. Some important results have already been revealed [150], demonstrating inhomogeneities on cell level, loss of mobile lithium and cathode overcharge:

(1) *Electrolyte filling level*: Hydrogen is a strong incoherent scatterer for neutrons and appears with high local neutron absorption contrast in neutron imaging. Therefore, the high hydrogen content of the electrolyte allows for a direct determination of the filling level and its changes as a function of state-of-charge (SOC) and with fatigue, see Fig. 24 and also [20].
(2) The loss of mobile Li is displayed in the composition of the overbalanced negative electrode, see Fig. 25. Only a small amount of LiC_{12} remains at the upper cut-off voltage, due to the slight graphite excess relative to the $LiCoO_2$ cathode. In the fatigued cell much more LiC_{12} remains, reflecting less Li in the negative electrode.
(3) The composition Li_xCoO_2 of the positive electrode can drop below the critical Li-content $x = 0.5$. In commercial cells no reference electrode is used. Therefore, only the overall voltage can be controlled. A potential drift at the negative electrode can result in an overcharge of the positive electrode. Values of $x \sim 0.4$ and $x \sim 0.3$ have been determined for $LiCoO_2$ and $Li(Ni_{1/3}Co_{1/3}Mn_{1/3})O_2$ positive electrode materials in 18650-type cells [148,149]. Especially in fatigued cells the positive electrode can become intrinsically unstable in the fully charged state. The formation of the corresponding equilibrium states and stable phases is considered as a capacity-reducing step, because these phases will not (or only to a minor extend) take part in the successive cycling.

Most electrode materials suffer from dramatic volume changes or distortions in dependence on the state-of-charge (SOC). Electrode particles are in contact with each other, with current collector

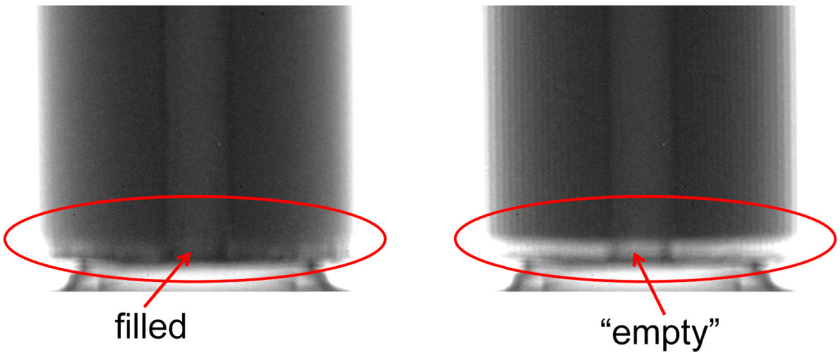

Fig. 24. Neutron absorption contrast in 18650-type Li-ion cells. In the charged state (left) the electrode volumes are larger and electrolyte is pressed out of the porous electrode structures. The bottom region appears in darker grey, because of the attenuation by electrolyte. In the discharged state (right) the electrolyte is soaked in the electrodes and a nearly electrolyte-free region appears. In addition the contrast between positive and negative electrodes changes significantly, because of the different Li-contents in the electrodes. A very similar Li-distribution exists in the charged state (main compositions are LiC_6 and $Li_{0.5}CoO_2$) in comparison to the discharged state (mainly Li-free graphite and $LiCoO_2$). Neutron absorption in the solids is mainly due to lithium, more precisely due to the 6Li isotope with a natural abundance of 7.5%.

and with electronic conductive additives, held together by polymer binders like polyvinylidene fluoride (PVDF). Cracks in the electrode particles can cause transport barriers for both, electrons and Li-ions, and even result in complete contact losses with accompanied inactivity of some parts of the electrodes. Such mechanical damage contributes to capacity losses by inactive regions and new surfaces, which consume Li-ions for the formation of additional SEI. Mechanical stresses caused by Li-extraction and -insertion as well as by changes in the coordination polyhedra of transition metals during oxidation and reduction have an important impact on fatigue, especially for brittle materials. Such bulk related effects can be most easily detected by structural studies as *e.g.* by diffraction techniques with electrons, X-rays and neutrons.

Two main methods are considered to define the level of degradation, also called the state-of-health (SOH). One is to compare the actual capacities during charge and discharge at fixed temperature, for the same rates and within the same voltage window with the initial values after formation. Another is to consider the relative change of the internal resistance, which will normally increase with fatigue in comparison to the fresh cell after formation. Both parameters do not allow identifying the main reasons for degradation. Many more parameters are needed and very often only *post mortem* studies can reveal more information about the underlying processes. For example only the cell voltage is measured and controlled, but not the individual potentials at the positive and negative electrode. The lack of a reference electrode in a normal commercial device is a serious limitation for the optimization

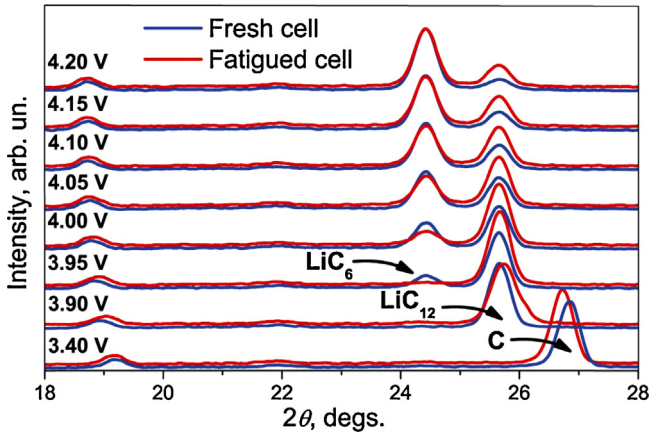

Fig. 25. Composition of the negative electrode in different SOCs, determined by the cell voltage and two different SOHs, fresh and fatigued after 1000 cycles.

of the operation conditions and the detection of the SOH during operation. Most powerful investigation methods are *in operando* techniques, because they can monitor fatigue and its proceeding in a non-invasive manner, exactly under the same conditions as during normal operation.

In the following, an example of spatially resolved Raman spectroscopy of electrode materials is illustrated, demonstrating the inhomogeneous nature of the composite cathode. Fig. 26 shows the results of a Raman mapping of a $LiCoO_2$ cathode composite (85% $LiCoO_2$, 10% PVDF, 5% carbon black) using green laser excitation at 532 nm [34]. The analysis of the mapping data reveals considerable chemical heterogeneity along the $LiCoO_2$ composite electrode with a complementary distribution of $LiCoO_2$ (top left) and carbon (bottom left). The variation in chemical composition is corroborated by the Raman spectra from different sample locations shown on the right of Fig. 26. Spatially resolved analysis is able to detect individual active mass particles of the $LiCoO_2$ composite. While the particles vary in size, they are typically in the range of ~10–20 μm.

Furthermore, spatially resolved Raman spectroscopy has been employed to study $LiCoO_2$ composite electrode before and after galvanostatic cycling at a rate of C/12. The Raman maps shown in Fig. 27 are based on Raman spectra taken at defined spots of the composite electrode with a step size of 5 μm thus sampling an area of 30 μm × 30 μm. The graphical images correspond to the integrated intensities of the A_{1g} phonon band of $LiCoO_2$ interpolated as colour gradients.

As before the Raman maps show a rather heterogeneous distribution of the chemical composition across the electrode surface. This behaviour is characteristic for all parts of the electrode surface examined. The spectra shown on the left were taken before galvanostatic cycling. However, it should be mentioned that the *in situ* cell was already fully assembled by that time, *i.e.* measurements were performed inside the *in situ* cell with the composite electrode and the electrolyte present. The right panel shows *in situ* Raman data after four galvanostatic cycles. Within the precision of the motorized stage (repeatability of 0.75 μm) the same area was under examination as before cycling. Importantly, comparison of the Raman maps before and after galvanostatic cycling shows a major redistribution of the chemical composition. This behaviour highlights the dynamic nature of $LiCoO_2$ composite electrodes under electrochemical conditions. Our findings are consistent with previous results on composite lithium-ion cathodes suggesting a rearrangement of carbon additives as well as formation of surface films during cycling. Such changes were postulated to contribute to the loss of contact resistances between particles leading to an overall degradation of the electrochemical performance.

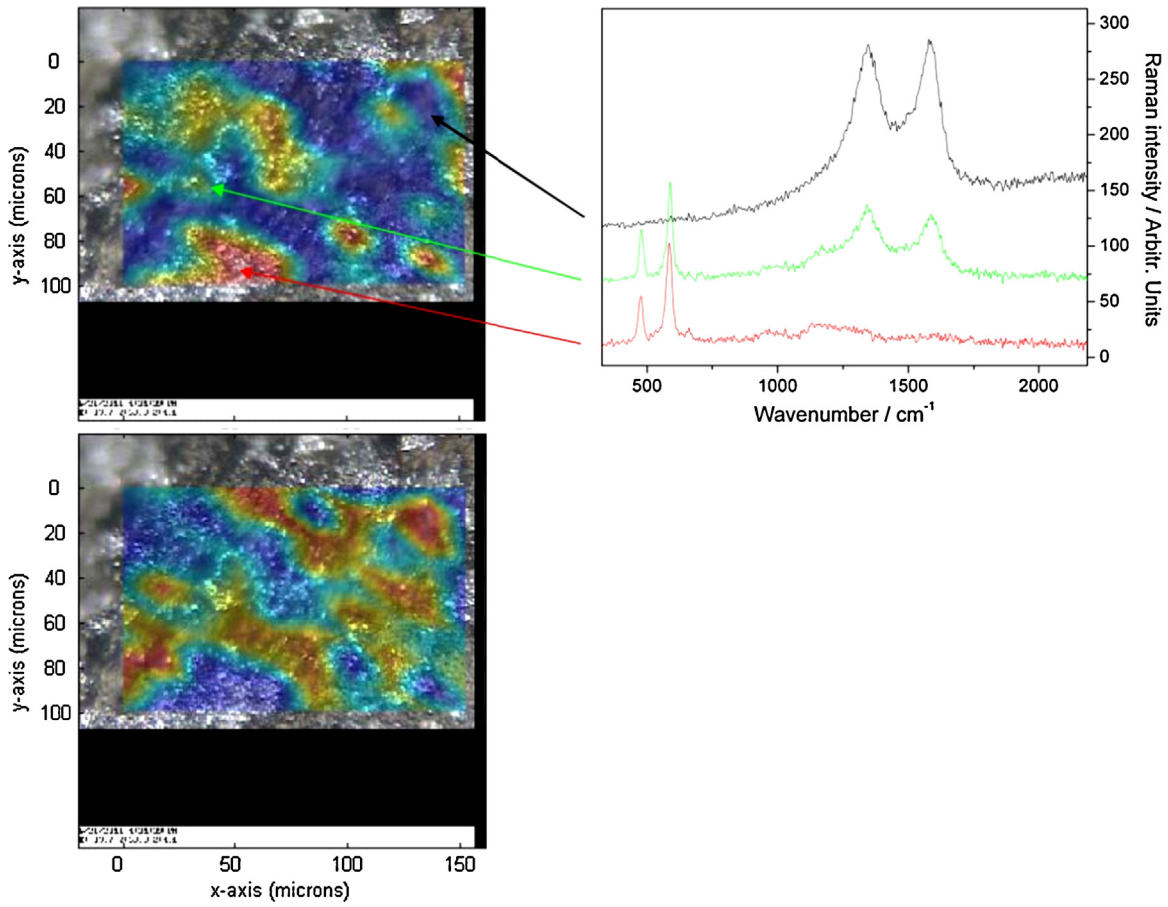

Fig. 26. Raman mapping of a cathode composite (85% $LiCoO_2$, 10% PVDF, 5% carbon black) overlaid onto the corresponding microscopy image showing the $LiCoO_2$ (top left image) and carbon (bottom left image) distribution. The Raman spectra (right image) correspond to the indicated points of the Raman map. Laser excitation at 532 nm was used. Spectra were offset for clarity [34]. A red colour in the mapping corresponds to a high amount of $LiCoO_2$ (top left image) or a high amount of carbon (bottom left). Reprinted from [34] with permission of Elsevier.

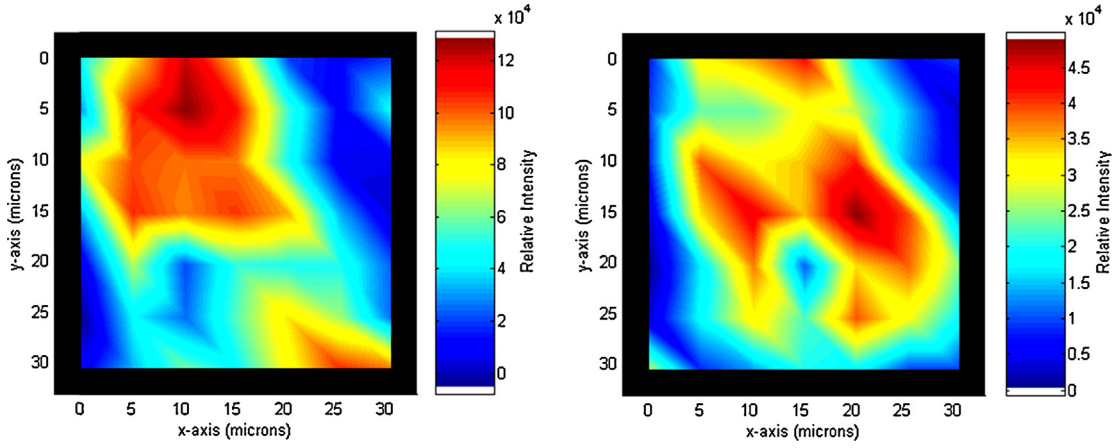

Fig. 27. *In situ* Raman maps of the same sample area of a $LiCoO_2$ composite electrode immersed into electrolyte before (left) and after (right) four electrochemical cycles. For excitation 532 nm laser emission was used. Signals correspond to integrated areas of the 595 cm^{-1} $LiCoO_2$ band after background subtraction [35].

8. New materials and approaches: solid state electrolytes and thin film cells

The stability of the electrolyte in contact with the electrodes during storage and operation is a key issue for the degradation of Li-ion batteries. A prominent degradation route is the decomposition of (liquid) electrolyte at anode and cathode, which eventually leads to increase of resistance and capacity fade due to loss of free lithium.

Electrolyte-related degradation may be minimized by the use of inorganic solid electrolytes. Such electrolytes have generally high stability, *i.e.* a large electrochemical stability window, and sustain only Li-ion mobility [151]. Any products from residual reactions are retained at the interfaces, and cells with lithium anodes show very high cycling stability [151–153]. Therefore, all-solid state batteries are envisioned as next generation lithium batteries with increased capacity, lifetime and safety [151]. Also, the use of inorganic solid

electrolytes as protective layers for cathodes and anodes in conventional Li-ion cells with liquid electrolytes is attractive, due to their high ionic but very low electronic conductivity.

8.1. Solid state electrolytes

There are a number of solid state electrolytes with high ionic conductivity even at room or slightly elevated temperatures [154], and material development is ongoing. Solid electrolytes with very high conductivity (10^{-3} S/cm at RT) are crystalline oxide-based or glassy sulphide-based materials [151,154]. Persisting issues regarding the use of solid electrolytes in Li-ion cells are high interface resistance and reactivity with electrode materials. This especially applies to sulphide-based systems, which face issues even when typical electrode materials such as $LiCoO_2$ or graphite are used [151], but also to oxide-based systems for the lithium anode or high-voltage cathodes [151,155]. It has been shown, however, that high interface resistance can be overcome by different treatments [155,156], but a rational interface design is still lacking.

Glassy oxide-based electrolytes find currently often application in planar thin film batteries [151,157,158], and have promising properties when used as artificial SEI-layer [133,159,160]. Generally glassy oxide-based electrolytes possess high stability, reasonable conductivities (up to several 10^{-6} S/cm at RT) and do not exhibit kinetic inhibitions due to structural misfits at the interfaces. A prominent feature of glassy electrolytes are local variations in conductivity, manifesting themselves *e.g.* in thickness-dependent conductivity [161].

A prominent example of this class of solid electrolytes is LiPON, which was first reported by Bates and co-workers [162]. It has been used successfully in thin film cells for quite some time [152], but also possesses promising properties as protective layer in liquid electrolyte cells [133,159,160]. LiPON is a nitrogen-substituted lithium phosphate glass with a limited network due to bridging and double-bonded oxygen (Ob and Od, respectively) and triple as well as double coordinated nitrogen (Nt and Nd, respectively) [162]. Typically, LiPON is deposited as thin film by rf-magnetron sputter deposition at room temperature using Li_3PO_4 as target and nitrogen as reactive gas [163]. For the typical composition of $Li_{2.9}PO_{3.3}N_{0.36}$, the ion conductivity of LiPON thin films is 2×10^{-6} S/cm at room temperature (RT) with negligible electronic conductivity (<10–14 S/cm) [163]. In fact, the composition range in which reasonable (ion) conductivities (around 10^{-6} S/cm at RT) are observed is quite large [164,165]. The comparable high conductivity is related to the incorporation of nitrogen [163], but the exact conduction mechanism is still under debate [166].

8.2. Thin film electrodes

Various thin film electrodes have been used in thin film cells [158,167] or as model electrodes for fundamental investigations [40,168,169]. Thin film deposition is a non-equilibrium process, and the deposition of stoichiometric materials with low defect concentrations is a challenge. On the other hand, thin film technologies offer the possibility to synthesize materials with an increased range of composition, given suitable deposition processes are used.

Thermodynamic stability *vs.* growth conditions is a key technological aspect for the successful preparation and life time of the $LiMO_2$ (M = Ni, Co, Mn) thin film layered cathode materials by using radio frequency (RF) film deposition techniques [42,127,128,170]. The film has to be well crystallized and stoichiometric with respect to lithium and oxygen contents to obtain a defined electronic configuration of the M atoms. $Li_{1.0}Co^{3+}{}_{1.0}O_2$ (LCO) is a "friendly" material for the thin film growth. The Co^{3+} ($3d^6$, $t_{2g}{}^3\uparrow t_{2g}{}^3\downarrow e_g{}^0$) with low spin (LS) state configuration is stable at various temperatures of film growth [42,127,128]. The high temperature (HT) phase of

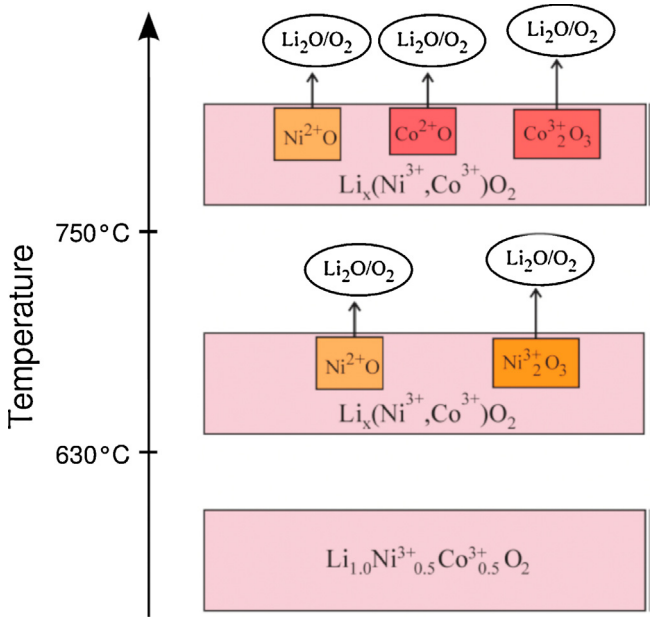

Fig. 28. Illustration of influence of temperature on the composition during phase formation in a LNCO film [127].

stoichiometric $LiCoO_2$ film is formed at $T = 400$–650 °C. A well crystallized stoichiometric HT-$LiCoO_2$ film cathode material exhibits good reversibility of the electrochemical properties up to 4.2 V *vs.* lithium restricted by the intrinsic voltage limit of $LiCoO_2$ material. Advantages of $LiNi^{3+}O_2$ (LNO) compared to LCO are a slightly higher theoretical capacity (275 mA h g^{-1} compared to 248 mA h g^{-1} for $LiCoO_2$ [171]), reduced cost and, as discussed before, a more stable electronic configuration at the higher voltage charged state compared to its cobalt counterpart. However, these advantages are offset by an instability of Ni^{3+}($3d^7$, $t_{2g}{}^3\uparrow t_{2g}{}^3\downarrow e_g{}^1\uparrow$) in the LS state ions. This leads at elevated growth temperatures to Li-deficiency, oxygen loss and $Ni^{2+} \leftrightarrow Li^+$-cation exchange in the as prepared film (see Fig. 28). Moreover, Ni^{2+} ions occupy the empty Li-sites during Li^+ deintercalation resulting in rapid cathode degradation. All these drawbacks lead to capacity fade and fast deterioration. A substitution of the Ni^{3+} ions by Co^{3+} ions resulting in $Li_{1.0}Ni^{3+}{}_{0.5}Co^{3+}{}_{0.5}O_2$ (LNCO) helps to stabilize the electronic structure and stoichiometry of the LNCO film against thermally induced oxygen loss and Li-deficiency.

To control the stoichiometry during LNCO film growth, a RF co-sputtering method has been developed to grow stoichiometric $LiMO_2$ films [127]. $Li(Ni^{2+},Co^{3+},Mn^{4+})O_2$ (LMNCO) has a higher voltage window compared to LCO and LNCO cathode materials, since the Mn^{4+}($3d$) state lowers the O($2p$) band with respect to the $Co^{2+/3+}$ and $Ni^{2+/3+/4+}$ redox couples due to inductive effects, thereby stabilizing the electronic structure of the layered oxide at a high charged state [6]. Similar to LNO and LNCO, the growth of a well crystallized stoichiometric LMNCO thin film cathode is not trivial task but RF co-sputtering technique is a proper tool to overcome the usual problems associated with non-stoichiometry and variation of oxidation state of the transition metals [129]. In order to obtain a well crystallized structure of Ni-based layered oxides, the temperatures during film growth have to be shifted to the higher values compared to $LiCoO_2$. However, the probability to form non-stoichiometric oxide phases in a LMNCO film increases with temperature. Therefore, the stability of the stoichiometric layered structure needs to be governed by control of the oxygen partial pressure during film growth and during annealing conditions. Fig. 29 illustrates the electrochemical properties of respective thin films.

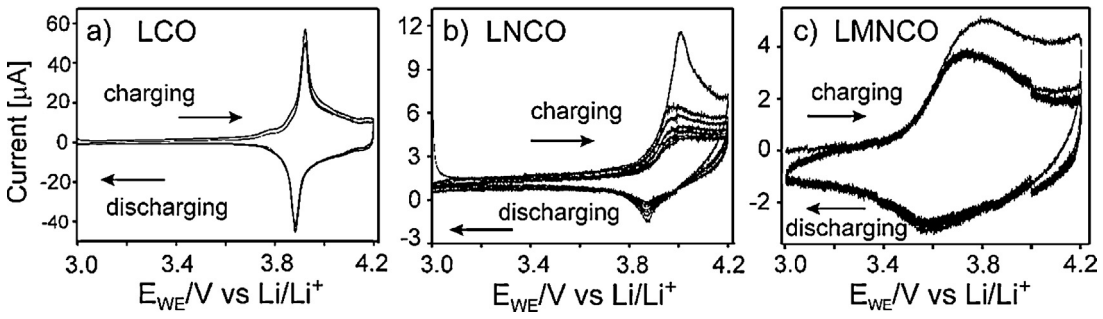

Fig. 29. Cyclic voltammograms (CV) of $LiCoO_2$ (LCO), $Li(Ni,Co)O_2$ (LNCO) and $Li(Mn,Ni,Co)O_2$ (LMNCO) thin film cathodes grown at $T = 550\,^{\circ}C$ (LCO), 750 °C (LNCO) and 600 °C (LMNCO), respectively. Lithium foil was used as anode and carbonate-based liquid electrolytes in a Swagelok LIB cell. Left and middle figure reproduced from [127] with permission of The Royal Society of Chemistry.

8.3. Thin film cells

Thin film cells with LiPON show excellent properties, such as high cycle stability and low self-discharge, and have been extensively investigated in planar geometry [157]. However, the capacity of such planar cells remains low (typically <250 µAh/cm^2) due to a limitation for the cathode film thickness [167]. In order to increase the capacity various concepts based on 3-D structures or 3-D surface structured substrates have been proposed [172]. Until now, however, the realization of such 3-D structured thin film cells is impeded by the lack of conformal, chemical vapour deposition-based processes, especially for the electrolyte. Only recently, first reports regarding the deposition of LiPON by chemical vapour deposition (CVD) have appeared [173,174].

A significant inner resistance is encountered for LiPON-based thin film cells, which can be attributed mostly to the resistance of the electrode/electrolyte interfaces, especially when high voltage cathodes are used [152,155]. Interface resistances may be due to high transfer resistances or due to the formation of reaction layers, and can be easily investigated by interface experiments for solid–solid contacts.

Such experiments demonstrate for the $LiCoO_2$/LiPON interface [51] that the chemical structure of LiPON is significantly different from inside the film as reflected in the changing ratios Ob/Od and Nt/Nd during deposition (Fig. 30), indicating that during growth the electrolyte adapts to the low lithium chemical potential (*i.e.* low Fermi-level) of the $LiCoO_2$ substrate. At the interface, the amorphous electrolyte is rich in triply bound nitrogen, which is taken as sign for a comparably high Li-ion conductivity in the interface region. No pronounced changes at the surface of $LiCoO_2$ are seen, and only minor band bending is observed indicating the absence of a large electric potential gradient at the interface. Therefore, we presume that the lithium (ion) chemical potential of $LiCoO_2$ and LiPON is comparable within a few tenth of eV, and that thermodynamic barriers for Li-ion transfer are of the same magnitude.

Determination of the valence band maximum offset *via* core level binding energies [52] yields 1.15 and 0.65 eV for LiPON deposited at room temperature and at 200 °C, respectively (Fig. 31). This dependence of the valence band offset on the deposition temperature is related to different valence band edges of the LiPON due to a different chemical structure (more nitrogen) when deposited at higher temperatures (see also [175,176]). The position of the Fermi level in $LiCoO_2$ above the valence band maximum and the high value(s) for the valence band maximum offset render the oxidation of LiPON for the fully lithiated $LiCoO_2$ unlikely.

The interface between LiPON (amorphous model structure obtained using USPEX) and $LiCoO_2$ ((0 0 0 1)-surface, half-Li termination) was also investigated by DFT calculations. In Fig. 32 it is shown how this interface is formed and that the electronic properties in the interface region, reflected in the density of states, are

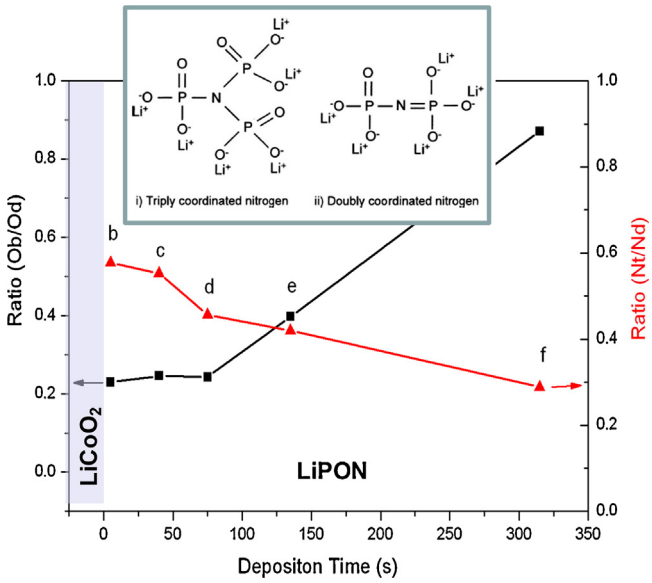

Fig. 30. Structural differences of LiPON near the interface region with $LiCoO_2$ as observed from an interface experiment with $LiCoO_2$ as substrate. Reprinted from [51] with kind permission of Springer Science and Business Media.

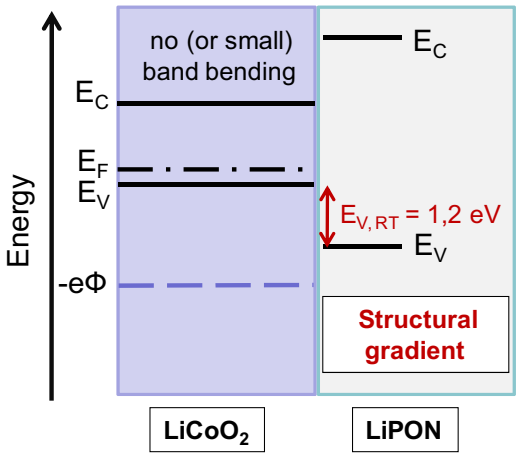

Fig. 31. Illustration of band diagram of $LiCoO_2$/LiPON interface, deduced from an interface experiment with $LiCoO_2$ as substrate. Note that minor downward band bending is observed in the $LiCoO_2$ (not shown). Reprinted from [142] with permission from Elsevier.

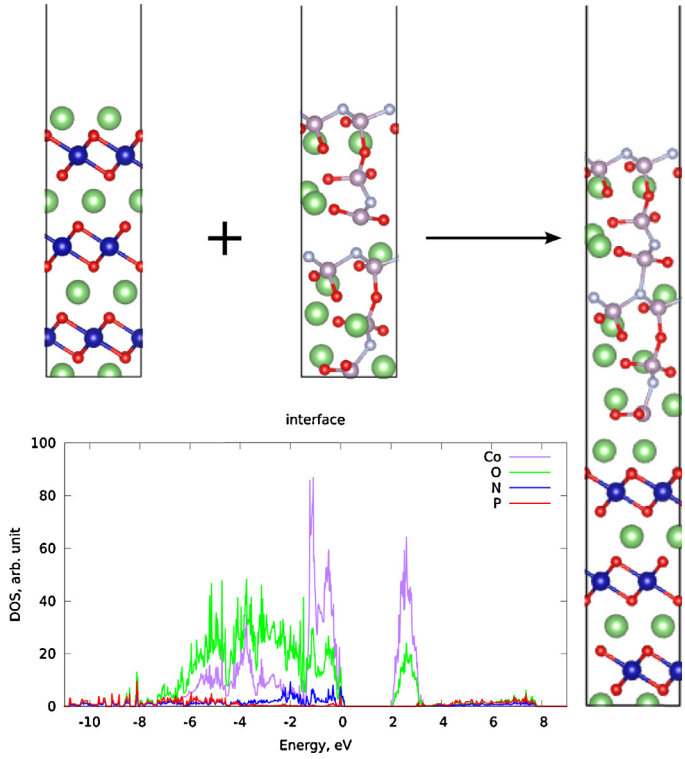

Fig. 32. Schematic representation of the formation of the interface between $LiCoO_2$ and LiPON slab models (including vacuum), and corresponding density of states.

dominated by the states of the cathode material. Major contributions to the upper valence band and conduction band originate from Co and O, no additional states can be found within the original band gap of $LiCoO_2$. Moreover, $LiCoO_2$ undergoes only minor structural changes upon interface formation with LiPON, consistent with experimental observations.

9. Summary

In this paper fundamental degradation mechanisms of Li-ion layered oxide cathode material have been reviewed and degradation on cell level has been addressed. It includes recent results obtained by novel *in situ*/*in operando* diffraction methods, modelling, and quasi *in situ* surface science analysis, as provided by investigations within our collaborative research effort (DFG SFB 595). Central are the evolution and interrelation of crystal structure, point defects and electronic structure of $LiMO_2$ (M = Ni, Co, Mn) cathode materials and their interfaces as key factors for the decay of the system.

Degradation is mainly characterized by irreversible capacity loss (capacity fade) and increase in cell impedance both due to fatigue caused by cell operation (charge/discharge cycles) as well as ageing phenomena occurring at rest. The pronounced interactions between different components of the Li-ion cell require an evaluation on cell level. Various degradation phenomena are known, which reflect the fact that the operation of Li-ion cells occurs close to or outside the stability limits of almost all involved phases and materials (*e.g.* electrolyte, electrodes, current collectors), causing (electro-)chemical side reactions and phase transformations.

Our recent results by *in situ* and *in operando* diffraction methods on commercial cells show that especially three, partly interrelated mechanisms deserve attention: degradation of the cathode due to overcharge, interface layer formation and loss of free lithium. Interface layer (SEI) formation and related electrolyte decomposition result in a constant loss of free lithium and continuous resistance increase. The loss of free lithium eventually leads to (positive) potential shift of the anode, leading to cathode overcharge, which promotes degradation of active cathode material and cracking of grains. We demonstrate in this contribution for $LiCoO_2$ as prototype material how oxygen loss and eventual phase transformation relates to changes in electronic structure and to point defect formation. The point defect concentration in the volume of a cathode material is imprinted during synthesis, and evolves during operation of the cell according to defect formation energies and defect mobility. During normal operation of the cathode, only lithium vacancies are formed and annihilated upon lithium (de)insertion. Upon overcharge, however, other point defects related to oxygen and transition metal(s) are also formed and lead to degradation.

For layered oxide cathodes oxygen-related defects such as oxygen vacancies play a major role for decomposition at low lithium content, but also defects related to transition metal ions (anti-sites and vacancies) can be crucial for the cathode stability. Particularly, for $LiCoO_2$ low or negative defect formation energies are found for oxygen vacancies and cobalt anti-site defects, implying that formation will take place, certainly on long time scales.

Next to defect formation energies, the stability of $LiMO_2$ cathode materials is linked to the evolution of electronic structure resulting from removal of electrons upon delithiation. Below a critical lithium composition electrons are removed from orbitals of predominantly oxygen 2*p* type character (hole formation) leading to oxygen loss and phase destabilization (oxidative decomposition). This transition is also evidenced in structural data as rapid shrinking of the *c*-axis parameter. It defines the stability limit of layered oxide cathode materials. The evolution of the electronic structure of transition metal oxides with varying lithium content explains the electrode stability depending on the electrode potential, leading to concepts such as the intrinsic voltage limit of cathode materials. Our analysis of thin film $LiCoO_2$ and $Li(Co,Ni)O_2$ electronic structure supports these concepts.

The formation of electrode/electrolyte reaction layers (SEI-layers) is a key process leading to capacity fade and resistance increase. The cathode SEI consists of an inorganic electrode surface layer as a result of cathode surface deterioration, covered by a layer of organic and inorganic compounds formed by electrolyte decomposition products. Surface deterioration and electrochemical electrolyte decomposition (electrolyte oxidation) are a consequence of the lack of electrochemical equilibrium at the interface for electrons, oxygen ions and transition metal ions. SEI formation is especially linked to electron transfer, which in turn is governed by the electronic energy alignment and contact potential at the interface. Not much attention has been paid in the past to these matters, which is attributed to experimental difficulties. Our surface science approach allows to evaluate energy alignment, contact potential and reactivity. On basis of the large electronic energy off-set at a $LiCoO_2$-solvent (*i.e.* DEC) interface as obtained by model experiments it is concluded that double layer formation and presence of salt significantly influence the oxidation of solvent. Also, evidence is found that charge carrier concentration changes and electric potential gradients at the interface due to the semiconducting nature of $LiCoO_2$ should be taken into account in the discussion of surface layer formation during handling, composite electrode fabrication and early cycling.

The degradation mechanisms addressed in this contribution indicate that capacity fade may be significantly slowed down if anodes with a stable potential and/or anodes containing lithium are employed. Loss of lithium and increase of inner resistance on the other hand require stable electrode/electrolyte interfaces. Both capacity fade and side reactions at electrode/electrolyte interfaces may be overcome by the use of suitable solid-state electrolytes and lithium anodes, as implied by the high cycling stability of thin film

cells. Life time can also be prolonged if less than the full reversible cathode capacity is addressed at the beginning of cell life, which may be an interesting option in the future considering ongoing development of higher capacity cathode materials.

Acknowledgements

The financial support from the German Science Foundation (DFG) of the collaborative research center SFB 595 "Electrical fatigue in functional materials" for three funding periods (2003–2014) is gratefully acknowledged. The authors thank all former and present colleagues who contributed to this work, namely I. Balog, D. Becker, N. Bramnik, C. Braun, H. Bremes, T. Buhrmester, M. Diehm, O. Dolotko, D. Ensling, C. Fasel, H. Fueß, M. Graczyk-Zajac, T. Gross, J. Kaspar, R. Kolb, So. Laubach, St. Laubach, D. Mikhailova, M. Mühlbauer, K. Nikolowski, P. C. Schmidt, V. Pradeep, L. Reinold, R. Riedel, J. Rohrer, S. Schmid, A. Senyshyn, S. Sicolo, F. Sigel, A. Thissen, M. Wilamowska.

References

[1] P.G. Bruce, B. Scrosati, J.M. Tarascon, Angew. Chem. Int. Ed. 47 (16) (2008) 2930–2946.
[2] B. Scrosati, J. Garche, J. Power Sources 195 (9) (2010) 2419–2430.
[3] J.M. Tarascon, Phil. Trans. R. Soc. A 368 (1923) (2010) 3227–3241.
[4] J.-K. Park, Principles and Applications of Lithium Secondary Batteries, Wiley-VCH, Weinheim, 2012.
[5] J.B. Goodenough, Y. Kim, Chem. Mater. 22 (3) (2010) 587–603.
[6] J.B. Goodenough, K.S. Park, J. Am. Chem. Soc. 135 (4) (2013) 1167–1176.
[7] H. Gerischer, F. Decker, B. Scrosati, J. Electrochem. Soc. 141 (9) (1994) 2297–2300.
[8] W.R. McKinnon, in: P.G Bruce (Ed.), Solid State Electrochemistry, Cambridge University Press, Cambridge, 1995.
[9] G. Liu, et al., J. Electrochem. Soc. 154 (12) (2007) A1129–A1134.
[10] M. Manickam, M. Takata, Electrochim. Acta 48 (2003) 957–963.
[11] J. Vetter, et al., J. Power Sources 147 (1–2) (2005) 269–281.
[12] F. German, et al., J. Power Sources 264 (2014) 100–107.
[13] D. Aurbach, et al., J. Electrochem. Soc. 147 (4) (2000) 1322–1331.
[14] K. Edstroem, T. Gustafsson, J.O. Thomas, Electrochim. Acta 50 (2004) 397–403.
[15] J. Maier, Physical Chemistry of Ionic Materials, John Wiley and Sons Ltd, Chichester, 2004.
[16] W. Weppner, Ionics 7 (4–6) (2001) 404–424.
[17] J. Maier, Phys. Chem. Chem. Phys. 11 (17) (2009) 3011–3022.
[18] W. Weppner, in: C.a.S.Z. Julien (Ed.), Materials for Lithium-Ion Batteries, Kluwer Academic Publishers, Dordrecht, 1999, pp. 401–412.
[19] M. Balkanski, Sol. Energy Mater. Sol. Cells 62 (1–2) (2000) 21–35.
[20] M. Lanz, et al., J. Power Sources 101 (2) (2001) 177–181.
[21] S.K. Jung, et al., Adv. Energy Mater. 4 (1) (2014) (Article no. 1300787).
[22] M. Ebner, et al., Science 342 (6159) (2013) 716–720.
[23] D. Aurbach, et al., J. Power Sources 165 (2) (2007) 491–499.
[24] K. Yamamoto, et al., J. Phys. Chem. C 118 (2014) 9538–9543.
[25] F. Lin, et al., Nat. Commun. 5 (2014) (Article no. 3529).
[26] H. Ehrenberg, et al., in: E.J. Mittemeijer, U. Welzel (Eds.), Modern Diffraction Methods, Wiley-VCH, 2012.
[27] M. Knapp, et al., Nucl. Instrum. Methods Phys. Res. Sect. A 521 (2–3) (2004) 565–570.
[28] M. Herklotz, et al., J. Appl. Crystallogr. 46 (2013) 1117–1127.
[29] C. Baehtz, et al., Solid State Ionics 176 (17–18) (2005) 1647–1652.
[30] K. Nikolowski, et al., J. Appl. Crystallogr. 38 (2005) 851–853.
[31] M. Hoelzel, et al., Neutron News 18 (2007) 23–26.
[32] O. Dolotko, et al., J. Electrochem. Soc. 159 (12) (2012) A2082–A2088.
[33] T. Gross, L. Giebeler, C. Hess, Rev. Sci. Instrum. 84 (7) (2013) (Article no. 073109).
[34] T. Gross, C. Hess, J. Power Sources 256 (2014) 220–225.
[35] T. Gross, C. Hess, ECS Trans. 61 (12) (2014) 1–9.
[36] K. Dokko, et al., J. Mater. Chem. 12 (12) (2002) 3688–3693.
[37] M. Kerlau, et al., Electrochim. Acta 52 (17) (2007) 5422–5429.
[38] R.J.H. Clark, T.J. Dines, Angew. Chem. Int. Ed. Engl. 25 (2) (1986) 131–158.
[39] L. Daheron, et al., Chem. Mater. 20 (2) (2008) 583–590.
[40] D. Takamatsu, et al., J. Phys. Chem. Lett. 2 (20) (2011) 2511–2514.
[41] H. Konishi, et al., J. Power Sources 246 (2014) 365–370.
[42] D. Ensling, et al., Phys. Rev. B 82 (19) (2010) (Article no. 195431).
[43] S. Hüfner, Photoelectron Spectroscopy, Springer-Verlag, Berlin, 2003.
[44] A. Thissen, et al., Ionics 15 (4) (2009) 393–403.
[45] Q.H. Wu, A. Thissen, W. Jaegermann, Surf. Sci. 578 (1–3) (2005) 203–212.
[46] S. Laubach, et al., Phys. Chem. Chem. Phys. 11 (17) (2009) 3278–3289.
[47] W. Jaegermann, D. Tonti, New Trends Intercal. Comp. Energy Storage 61 (2002) 289–354.
[48] D. Tonti, C. Pettenkofer, W. Jaegermann, Ionics 6 (3–4) (2000) 196–202.
[49] G. Cherkashinin, et al., Phys. Chem. Chem. Phys. 14 (35) (2012) 12321–12331.
[50] D. Becker, et al., J. Phys. Chem. C 118 (2) (2014) 962–967.
[51] S. Jacke, et al., Ionics 16 (9) (2010) 769–775.
[52] J. Song, et al., Electrochem. Solid State Lett. 14 (12) (2011) A189–A191.
[53] A. Klein, et al., Bunsen-Magazin 10 (4) (2008) 124–139.
[54] V. Ramadesigan, et al., J. Electrochem. Soc. 159 (3) (2012) R31–R45.
[55] A. Barre, et al., J. Power Sources 241 (2013) 680–689.
[56] M. Landstorfer, T. Jacob, Chem. Soc. Rev. 42 (8) (2013) 3234–3252.
[57] W. Kohn, L.J. Sham, Phys. Rev. A 140 (4) (1965) 1133.
[58] P. Hohenberg, W. Kohn, Phys. Rev. B 136 (3) (1964) B864.
[59] A.R. Oganov, C.W. Glass, J. Chem. Phys. 124 (24) (2006) 244704.
[60] C.W. Glass, A.R. Oganov, N. Hansen, Comput. Phys. Commun. 175 (11–12) (2006) 713–720.
[61] D. Morgan, G. Ceder, S. Curtarolo, Meas. Sci. Technol. 16 (1) (2005) 296–301.
[62] A. Jain, et al., Comput. Mater. Sci. 50 (8) (2011) 2295–2310.
[63] G. Hautier, et al., Chem. Mater. 23 (15) (2011) 3495–3508.
[64] R.J. Gummow, A. de Kock, M.M. Thackeray, Solid State Ionics 69 (1994) 59–67.
[65] J.R. Dahn, et al., Solid State Ionics 69 (3–4) (1994) 265–270.
[66] K. Nikolowski, et al., ECS Trans. 26 (2006) 17–26.
[67] N. Kiziltas-Yavuz, et al., Electrochim. Acta 113 (2013) 313–321.
[68] K. Nikolowski, In situ Strukturuntersuchungen an Li(Ni, Co)O_2 als Kathodenmaterial für Lithiumionenbatterien, Department of Materials Science, Darmstadt University of Technology, Darmstadt, 2007.
[69] D. Rafaja, V. Klemm, M. Dopita, Newl. Comm. Powder Diffr. 34 (2007) 7–12.
[70] L. Wang, T. Maxisch, G. Ceder, Chem. Mater. 19 (3) (2007) 543–552.
[71] Y. Kim, D. Kim, S. Kang, Chem. Mater. 23 (24) (2011) 5388–5397.
[72] G. Kresse, J. Hafner, Phys. Rev. B 48 (17) (1993) 13115–13118.
[73] G. Kresse, J. Furthmüller, Comput. Mater. Sci. 6 (1) (1996) 15–50.
[74] G. Kresse, J. Furthmüller, Phys. Rev. B 54 (16) (1996) 11169–11186.
[75] G. Kresse, D. Joubert, Phys. Rev. B 59 (3) (1999) 1758–1775.
[76] P.E. Blöchl, Phys. Rev. B 50 (24) (1994) 17953–17979.
[77] D.M. Ceperley, B.J. Alder, Phys. Rev. Lett. 45 (7) (1980) 566–569.
[78] D. Kramer, G. Ceder, Chem. Mater. 21 (16) (2009) 3799–3809.
[79] G.G. Amatucci, J.M. Tarascon, L.C. Klein, Solid State Ionics 83 (1–2) (1996) 167–173.
[80] T. Motohashi, et al., J. Appl. Phys. 103 (7) (2008).
[81] S. Kawasaki, et al., Phys. Rev. B 79 (22) (2009).
[82] Y. Baba, S. Okada, J. Yamaki, Solid State Ionics 148 (3–4) (2002) 311–316.
[83] J. Yamaki, et al., J. Power Sources 119 (2003) 789–793.
[84] H. Gabrisch, Y. Ozawa, R. Yazami, Electrochim. Acta 52 (4) (2006) 1499–1506.
[85] H. Gabrisch, M. Kombolias, D. Mohanty, Solid State Ionics 181 (1–2) (2010) 71–78.
[86] A. Artemenko, et al., J. Appl. Phys. 106 (6) (2009) 064914.
[87] J. Reed, G. Ceder, Chem. Rev. 104 (10) (2004) 4513–4533.
[88] M. Catti, Phys. Rev. B 61 (3) (2000) 1795–1803.
[89] A. Van der Ven, et al., Phys. Rev. B 6418 (18) (2001) 184307.
[90] R. Gupta, A. Manthiram, J. Solid State Chem. 121 (2) (1996) 483–491.
[91] R.V. Chebiam, F. Prado, A. Manthiram, Chem. Mater. 13 (9) (2001) 2951–2957.
[92] J.M. Tarascon, et al., J. Solid State Chem. 147 (1) (1999) 410–420.
[93] G. Ceder, M.K. Aydinol, Solid State Ionics 109 (1–2) (1998) 151–157.
[94] N. Imanishi, et al., Solid State Ionics 140 (1–2) (2001) 45–53.
[95] S. Levasseur, et al., Chem. Mater. 15 (1) (2003) 348–354.
[96] S. Levasseur, et al., Solid State Ionics 128 (1–4) (2000) 11–24.
[97] S.B. Zhang, J.E. Northrup, Phys. Rev. Lett. 67 (17) (1991) 2339–2342.
[98] P. Erhart, et al., Phys. Rev. B 76 (17) (2007).
[99] K. Hoang, M. Johannes, Chem. Mater. 23 (11) (2011) 3003–3013.
[100] D. Takamatsu, et al., Angew. Chem. Int. Ed. 51 (46) (2012) 11597–11601.
[101] Y. Koyama, et al., Chem. Mater. 24 (20) (2012) 3886–3894.
[102] Y. Koyama, et al., J. Power Sources 244 (2013) 592–596.
[103] H. Tukamoto, A.R. West, J. Electrochem. Soc. 144 (9) (1997) 3164–3168.
[104] L. Wang, et al., Phys. Rev. B 76 (16) (2007) 165435.
[105] Y. Kim, H. Lee, S. Kang, J. Mater. Chem. 22 (25) (2012) 12874–12881.
[106] R. Benedek, M.M. Thackeray, Phys. Rev. B 83 (19) (2011) 195439.
[107] A. Karim, S. Fosse, K.A. Persson, Phys. Rev. B 87 (7) (2013) 075322.
[108] P.M. Diehm, P. Agoston, K. Albe, ChemPhysChem 13 (10) (2012) 2443–2454.
[109] K. Iwaya, et al., Phys. Rev. Lett. 111 (12) (2013) 126104.
[110] H. Moriwake, et al., Adv. Mater. 25 (4) (2013) 618–622.
[111] H.H. Zheng, et al., J. Power Sources 207 (2012) 134–140.
[112] R.N. Methekar, et al., J. Electrochem. Soc. 158 (4) (2011) A363–A370.
[113] K. Leung, J.L. Budzien, Phys. Chem. Chem. Phys. 12 (25) (2010) 6583–6586.
[114] K. Leung, J. Phys. Chem. C 117 (4) (2013) 1539–1547.
[115] K. Leung, C.M. Tenney, J. Phys. Chem. C 117 (46) (2013) 24224–24235.
[116] K. Leung, et al., J. Electrochem. Soc. 161 (3) (2014) A213–A221.
[117] R. Jorn, et al., J. Phys. Chem. C 117 (8) (2013) 3747–3761.
[118] P. Ganesh, P.R.C. Kent, D.E. Jiang, J. Phys. Chem. C 116 (46) (2012) 24476–24481.
[119] J. Vanelp, et al., Phys. Rev. B 44 (12) (1991) 6090–6103.
[120] V.R. Galakhov, et al., Phys. Solid State 44 (2) (2002) 266–273.
[121] A.W. Moses, et al., Appl. Surf. Sci. 253 (10) (2007) 4782–4791.
[122] N.V. Kosova, et al., J. Power Sources 119 (2003) 669–673.
[123] B.C. Melot, J.M. Tarascon, Acc. Chem. Res. 46 (5) (2013) 1226–1238.
[124] A.R. West, Basic Solid State Chemistry, 2nd ed., John Wiley & Sons Ltd, Chichester, 2010.
[125] R.V. Chebiam, F. Prado, A. Manthiram, J. Solid State Chem. 163 (1) (2002) 5–9.
[126] D. Ensling, et al., Chem. Mater. 26 (13) (2014) 3948–3956.

[127] G. Cherkashinin, D. Ensling, W. Jaegermann, J. Mater. Chem. A 2 (10) (2014) 3571–3580.
[128] G. Cherkashinin, et al., Surf. Sci. 608 (2013) L1–L4.
[129] G. Cherkashinin et al., in preparation.
[130] D. Takamatsu, et al., J. Electrochem. Soc. 160 (5) (2013) A3054.
[131] Y. Takanashi, et al., J. Power Sources 196 (24) (2011) 10679–10685.
[132] L.J. Fu, et al., Solid State Sci. 8 (2) (2006) 113–128.
[133] J. Song, et al., Electrochem. Solid State Lett. 14 (2) (2011) A11–A13.
[134] S.J. Shi, et al., J. Power Sources 225 (2013) 338–346.
[135] D. Aurbach, et al., J. Power Sources 81 (1999) 95–111.
[136] N. Sato, Electrochemistry at Metal and Semiconductor Electrodes, Elsevier Science B.V., Amsterdam, 2003.
[137] W. Jaegermann, A. Klein, T. Mayer, Adv. Mater. 21 (42) (2009) 4196–4206.
[138] A.M. Andersson, et al., J. Electrochem. Soc. 149 (10) (2002) A1358–A1369.
[139] N. Liu, et al., Electrochem. Solid State Lett. 9 (7) (2006) A328–A331.
[140] D. Becker, et al., Solid State Ionics 230 (2013) 83–85.
[141] D. Becker, et al., J. Phys. Chem. C 118 (2) (2014) 962–967.
[142] R. Hausbrand, D. Becker, W. Jaegermann, Prog. Solid State Chem. (2014), http://dx.doi.org/10.1016/j.progsolidstchem.2014.04.010 (in press).
[143] L. Daheron, et al., J. Phys. Chem. C 113 (14) (2009) 5843–5852.
[144] N. Andreu, et al., J. Phys. Chem. C 116 (38) (2012) 20332–20341.
[145] R. Hausbrand, Phys. Status Solidi A 211 (9) (2014) 2049–2051.
[146] Y. Gong, et al., Nano Lett. 13 (2013) 4340–4345.
[147] M. Zier, et al., J. Power Sources 266 (2014) 198–207.
[148] A. Senyshyn, et al., J. Power Sources 203 (2012) 126–129.
[149] A. Senyshyn, et al., J. Power Sources 245 (2014) 678–683.
[150] O. Dolotko, et al., J. Power Sources 255 (2014) 197–203.
[151] K. Takada, Acta Mater. 61 (3) (2013) 759–770.
[152] J.B. Bates, et al., Solid State Ionics 135 (2000) 33–45.
[153] B. Wang, et al., J. Electrochem. Soc. 143 (10) (1996) 3203–3213.
[154] P. Knauth, Solid State Ionics 180 (14–16) (2009) 911–916.
[155] C. Yada, et al., LiBD-6 2013 Conference Proceedings, 2013.
[156] Y. Iriyama, et al., J. Electrochem. Soc. 153 (5) (2006) A821–A825.
[157] N.J. Dudney, Electrochem. Soc. Interface Fall (2008) 44–48.
[158] S. Jacke, J. Song, G. Cherkashinin, L. Dimesso, W. Jaegermann, 15th International Meeting on Lithium Batteries, IMLB, 2010, Montréal, Canada, 2010.
[159] N.J. Dudney, J. Power Sources 89 (2000) 176–179.
[160] Y. Kim, et al., J. Electrochem. Soc. 160 (5) (2013) A3113–A3125.
[161] F. Berkemeier, M.R.S. Abouzari, G. Schmitz, Phys. Rev. B 76 (2) (2007) (Article no. 024205).
[162] J.B. Bates, et al., Solid State Ionics 53 (6) (1992) 647–654.
[163] X.H. Yu, et al., J. Electrochem. Soc. 144 (2) (1997) 524–532.
[164] B. Fleutot, et al., Solid State Ionics 186 (1) (2011) 29–36.
[165] N. Suzuki, et al., Solid State Ionics 191 (1) (2011) 49–54.
[166] F. Munoz, J. Power Sources 198 (2012) 432–433.
[167] N.J. Dudney, Mater. Sci. Eng. B 116 (3) (2005) 245–249.
[168] K. Yamamoto, et al., Angew. Chem. Int. Ed. 49 (26) (2010) 4414–4417.
[169] D. Ensling, Materials Science, Darmstadt University of Technology, Darmstadt, 2006.
[170] D. Ensling, in: K. Zaghib, C.M. Julien, J. Prakash (Eds.), New Trends in Intercalation Compounds for Energy Storage Conversion, Proc. ECS, Paris, 2003.
[171] Y.W. Tsai, et al., Chem. Mater. 17 (12) (2005) 3191–3199.
[172] J.F.M. Oudenhoven, L. Baggetto, P.H.L. Notten, Adv. Energy Mater. 1 (1) (2011) 10–33.
[173] L. Meda, E.E. Maxie, Thin Solid Films 520 (6) (2012) 1799–1803.
[174] H.T. Kim, et al., J. Power Sources 244 (2013) 641–645.
[175] Y.J.A. Du, N.A.W. Holzwarth, Phys. Rev. B 81 (18) (2010) (Article no. 184106).
[176] A. Schwöbel, et al., Appl. Surf. Sci. (2014) (in press).